JOURNAL OF PETROLOGY

Journal of Petrology, 2015, Vol. 56, No. 8, 1585–1606
doi: 10.1093/petrology/egv046
Original Article

OXFORD

An Experimental Study of Trace Element Fluxes from Subducted Oceanic Crust

L. B. Carter[1,2], S. Skora[1,3]*, J. D. Blundy[1], J. C. M. De Hoog[4] and T. Elliott[1]

[1]School of Earth Sciences, University of Bristol, Wills Memorial Building, Queen's Road, Bristol BS8 1RJ, UK, [2]Department of Earth Science, Rice University, 6100 Main Street, Houston, TX 77005, USA, [3]Department Erdwissenschaften, ETH Zürich, Clausiusstrasse 25NW, 8092 Zürich, Switzerland, [4]School of GeoSciences, University of Edinburgh, Grant Institute, The King's Buildings, James Hutton Road, Edinburgh EH9 3FE, UK

*Corresponding author. E-mail: Susanne.Skora@erdw.ethz.ch

Received July 26, 2014; Accepted July 24, 2015

ABSTRACT

We have determined experimentally the hydrous phase relations and trace element partitioning behaviour of ocean floor basalt protoliths at pressures and temperatures (3 GPa, 750–1000°C) relevant to melting in subduction zones. To avoid potential complexities associated with trace element doping of starting materials we have used natural, pristine mid-ocean ridge basalt (MORB from Kolbeinsey Ridge) and altered oceanic crust (AOC from Deep Sea Drilling Project leg 46, ~20°N Atlantic). Approximately 15 wt % water was added to starting materials to simulate fluid fluxing from dehydrating serpentinite underlying the oceanic crust. The vapour-saturated solidus is sensitive to basalt K_2O content, decreasing from 825 ± 25°C in MORB (~0·04 wt % K_2O) to ≈750°C in AOC (~0·25 wt % K_2O). Textural evidence indicates that near-solidus fluids are sub-critical in nature. The residual solid assemblage in both MORB and AOC experiments is dominated by garnet and clinopyroxene, with accessory kyanite, epidote, Fe–Ti oxide and rutile (plus quartz–coesite, phengite and apatite below the solidus). Trace element analyses of quenched silica-rich melts show a strong temperature dependence of key trace elements. In contrast to the trace element-doped starting materials of previous studies, we do not observe residual allanite. Instead, abundant residual epidote provides the host for thorium and light rare earth elements (LREE), preventing LREE from being released (ΣLREE <3 ppm at 750–900°C). Elevated Ba/Th ratios, characteristic of many arc basalts, are found to be generated within a narrow temperature field above the breakdown temperature of phengite, but below exhaustion of epidote. Melts with Ba/Th >1500 and La/Sm_{PUM} (where PUM indicates primitive upper mantle) ~1, most closely matching the geochemical signal of arc lavas worldwide, were generated from AOC at 800–850°C.

Key words: arc volcanics; experimental petrology; MORB; partial melting; subduction

INTRODUCTION

Volcanic arc basalts are widely considered to form from a mantle wedge source region comprising a ternary mixture of hydrous melt from subducted sediment, hydrous fluid (or melt) from (altered) mafic oceanic crust and depleted mantle peridotite (e.g. Elliott, 2003). The distinct trace element chemistry of basalts from different arcs can be ascribed to differing proportions of these three components, reflecting a variation both in inputs to the subduction system and in its thermal structure. Consequently, the phase relations of the different subducted components are important to determining under what conditions fluids and melts are generated beneath arcs. If the pressure–temperature dependence of the stability of key residual phases in subducted lithologies can be quantified then potentially the trace element chemistry of arc basalts can be used to infer slab-top temperatures beneath volcanic arcs (e.g. Hermann & Spandler, 2008; Klimm *et al.*, 2008; Plank *et al.*, 2009; Cooper *et al.*, 2012). The primary

objective of this study is to explore the trace element chemistry of hydrous partial melts associated with ocean floor basalts under subduction zone conditions.

Subducted slabs contain H_2O in the form of hydrous minerals, such as amphibole, epidote, micas and serpentine. The breakdown of these minerals during subduction zone metamorphism leads to progressive dehydration of the slab, releasing hydrous fluids into the overlying mantle wedge (e.g. Schmidt & Poli, 1998). If slab temperatures are high enough, as suggested by recent models (e.g. van Keken *et al.*, 2002; Syracuse *et al.*, 2010), dehydration melting of the slab will occur, giving rise to hydrous, silica-rich melts that may similarly ascend into the wedge. Thus both fluid and melt may be extracted from the slab depending on the subduction zone geotherm. If each slab lithology behaves as a closed system during subduction zone metamorphism, the only H_2O available in subducted basalt is that structurally bound in hydrous minerals in the basalt itself. Dehydration melting of such basalt occurs at relatively high temperatures that may be achieved only where the subducted crust is young and therefore hot. Consequently, there is a longstanding debate as to whether sub-solidus fluids or supra-solidus hydrous melts are the primary agent of slab–wedge chemical transfer in subduction zones. Such a simple dichotomy is complicated by the fact that at sufficiently high pressures silicate melts and hydrous fluids are completely miscible (above the so-called second critical endpoint) rendering moot any distinction between fluid and melt. Moreover, the dehydration of serpentine in ultramafic portions of the slab (Ulmer & Trommsdorff, 1995) may flux overlying basaltic and sedimentary portions with H_2O, such that dehydration melting of subducted basalt may not be the only melt-producing mechanism. More in-depth summaries of subduction zone processes can be found in the recent reviews of Spandler & Pirard (2013) and Schmidt & Poli (2014). Our experiments were designed explicitly to test this flux-melting mechanism by using starting materials in which H_2O contents exceeded those that could be contained within hydrous minerals alone. In that sense our experiments build upon those of Ryabchikov *et al.* (1996), Prouteau *et al.* (1999, 2001), Kessel *et al.* (2005*a*, 2005*b*) and Klimm *et al.* (2008).

To replicate experimentally the phase relations of hydrous ocean floor basalts it is important to take account of the chemical effects of alteration that occur on the sea floor. Subducted basalts range in composition from pristine mid-ocean ridge basalts (MORB), unmodified since eruption, to hydrothermally modified, altered oceanic crust (AOC) that characterizes the upper pillow lavas and sheeted dykes (e.g. Alt *et al.*, 1989). The nature of sea-floor alteration depends on the temperature of hydrothermal interaction (e.g. Humphris & Thompson, 1978; Mottl, 1983; Thompson, 1983) and, although its chemical signature is spatially variable, both laterally and vertically (e.g. Kelley *et al.*, 2003), the key chemical changes relative to MORB are an overall rise in alkalis and the volatile components sulphur, water and carbon dioxide, and to a lesser extent uranium (e.g. Melson, 1968; Staudigel *et al.*, 1981*a*, 1981*b*; Mottl, 1983; Gillis & Robinson, 1988; Seyfried *et al.*, 1988; Staudigel & Plank, 1996; Bach *et al.*, 2003; Kelley *et al.*, 2003). Previous experimental studies have attempted to capture this chemical variability by using either synthetic MORB (e.g. K-free MORB: Kessel *et al.*, 2005*a*, 2005*b*; KCMASH: Hermann & Green, 2001; anhydrous MORB: Yasuda *et al.*, 1994; altered MORB: Ryabchikov *et al.*, 1996; Klimm *et al.*, 2008) or metamorphosed material (e.g. amphibolite: Rapp & Watson, 1995; Kogiso *et al.*, 1997; synthetic eclogite: Klemme *et al.*, 2002; Pertermann & Hirschmann, 2003). In several cases the starting materials were doped with trace elements to facilitate trace element analysis of experimental run products and enhance the stability of accessory phases (e.g. Klimm *et al.*, 2008). The first aim of our study was to remove the uncertainties inherent in the use of synthetic and/or trace element-doped starting samples by using natural ocean floor basalts. The second aim was to explore changes in phase petrology and trace element partitioning that arises from chemical differences between MORB and AOC.

METHODS

Starting materials

Sample materials used for this study were splits of rock powder that were used for other geochemical studies. The first sample ('MORB') is a pristine MORB tholeiite (37DS-1) from the Kolbeinsey Ridge, retrieved from 67·08°N, 18·75°W between the Tjörnes and Spar fracture zones, at a depth of 170 m (Devey *et al.*, 1994). This sample is extremely fresh and unaltered, though slightly lower in TiO_2 and more depleted compared with average MORB given by Hofmann (1988; Table 1). Dredged basalts from this site are described as being mostly glassy with less than 10% (modal) phenocrysts (olivine and minor plagioclase and spinel for 37DS-1). The fO_2 of MORB is generally around the quartz–fayalite–magnetite (QFM) buffer, amounting to an average $Fe^{3+}/Fe^{tot} \approx 0{\cdot}16$ (e.g. Cottrell & Kelley, 2011).

The second sample ('AOC') is an altered basalt (15-3, A3, 83–94 cm) from Deep Sea Drilling Project (DSDP) leg 46 Hole 396B near the Mid-Atlantic Ridge at a latitude of 23°N and a depth of ~240 m. This horizon is not described in the Ocean Drilling Program (ODP) report, but comes from a massive lava stream of subunit A3. Other samples from this subunit are described as porphyritic basalts (~15–25% phenocrysts in leg 46 basalts), containing olivine and plagioclase phenocrysts with Ca-rich clinopyroxene in the groundmass and spinel. The massive lava is similar to overlying pillow basalts, which can show secondary palagonite, Fe–Mn oxide, smectite, mica, zeolite and carbonate (e.g. Dungan *et al.*, 1979; Sato *et al.*, 1979). The seafloor-metasomatized parts of the lava unit exhibit elevated concentrations of H_2O (≈2 wt %), K_2O (≈0·3 wt %), Fe_2O_3

Table 1: Starting compositions of basalts used in various experiments in comparison with natural compositions

Comp.:	'Pristine' MORB					'Altered' MORB (AOC)							
Study:	TS	TS	Dev94	Kess05a	Kess05b	TS	TS	LEG46	LEG46	Kelley03	Klimm08	G&A03	Hoff88
Type:	MORB	SD	37DS-1	Syn. MORB*	Syn. MORB	AOC	SD	A3-Av.	SD	Av. AOC Pacific	Syn. AOC*	Oc. tholeiite*	Av. MORB
Major elements (wt %)													
n	20	20	1	—	—	40	40	12	12	117	—	—	26
SiO_2	49·6	0·3	48·7	53·4	51·7	51·0	0·5	50·5	0·3	50·4	50·0	51·3	50·7
TiO_2	0·63	0·02	0·64	1·45	1·52	1·58	0·04	1·66	0·02	1·74	1·17	1·89	1·62
Al_2O_3	15·5	0·1	15·9	17·2	16·7	15·7	0·3	15·5	0·2	12·3	16·1	14·1	15·3
FeO_{tot}	8·9	0·2	10·1	8·50	9·98	9·6	0·2	10·0	0·2	12·5	11·7	12·2	10·5
MnO	0·18	0·04	0·18	—	—	0·13	0·03	0·20	0·01	0·23	0·10	0·19	—
MgO	10·3	0·1	10·1	5·93	7·03	7·4	0·1	7·7	0·3	6·36	7·16	6·55	7·62
CaO	13·0	0·1	12·7	10·2	9·92	11·0	0·1	10·9	0·1	13·3	10·2	10·5	11·4
Na_2O	1·83	0·08	1·71	3·24	3·17	3·3	0·1	3·0	0·1	2·35	3·31	2·80	2·69
K_2O	0·04	0·01	0·03	—	—	0·25	0·02	0·21	0·08	0·63	0·28	0·31	0·11
P_2O_5	0·05	0·02	0·04	—	—	n.d.	n.d.	0·14	0·01	0·17	—	0·22	—
Sum	100	—	100	100	100	100	—	100	—	100	100	100	100
Mg#	0·67	0·01	0·64	0·55	0·56	0·58	0·01	0·58	0·01	0·48	0·52	0·49	0·56
Trace elements (ppm)													
n	5	5	1	—	—	5	5	4–12	4–12	117	—	—	26
Li	3·39	0·07	—	247	—	33·3	0·1	13	12	14·1	92	82·6	—
Sc	47	1	—	148	—	41·8	0·8	38	1	37·4	83	—	41·4
Ti	3880	60	—	8590	—	9034	248	9822	113	—	7010	11300	9740
V	265	6	—	—	—	233	4	282	5	338	48	355	—
Rb	0·7	0·2	0·58	84	—	4·4	0·5	1·9	1·1	13·7	—	102	1·26
Sr	56	1	55	113	—	214	3	137	5	109	36	210	113
Y	19·8	0·3	18·6	102	—	34	1	34·8	1·1	40·7	40	159	35·8
Zr	29·2	0·5	28	151	—	107	6	116	3	112	145	227	104
Nb	2·7	0·2	1·69	135	—	2·3	0·2	1·9	0·4	2·89	120	128	3·51
Cs	0·06	0·03	—	87	—	0·32	0·07	—	—	0·317	—	80·7	0·014
Ba	7·1	0·2	6·9	97	—	5·1	0·7	—	—	15·6	—	176	13·9
La	2·0	0·1	1·00	131	—	3·8	0·2	4·3	0·4	3·4	158	97·0	3·90
Ce	3·4	0·2	2·91	137	—	13	1	11·8	1·5	11·4	167	114	12·0
Nd	3·2	0·3	3·22	176	—	13	1	10·6	1·1	11·3	176	—	11·2
Sm	1·3	0·1	1·33	180	—	3·7	0·3	4·1	0·2	3·95	163	94·3	3·75
Eu	0·57	0·07	0·57	192	—	1·2	0·1	1·32	0·02	1·34	207	—	1·34
Gd	1·26	0·09	2·05	220	—	4·9	0·4	—	—	5·55	—	—	5·08
Dy	2·7	0·2	3·05	239	—	5·5	0·5	6·5	0·2	6·56	—	—	6·30
Lu	0·31	0·04	0·35	143	—	0·55	0·03	0·64	0·03	0·636	133	100	0·589
Hf	0·9	0·2	1·04	231	—	2·6	0·3	3·0	0·1	3·07	39	13·5	2·97
Ta	0·34	0·02	—	120	—	0·17	0·03	0·20	0·01	0·21	36	11·2	0·192
Th	0·13	0·01	—	229	—	0·14	0·03	0·15	0·01	0·173	268	106	0·187
U	0·06	0·03	—	241	—	0·08	0·02	—	—	0·390	257	102	0·071
∑LREE	9·9	0·4	8·5	624	—	33	2	31	2	30	664	305	31

*Trace element doped compositions.

Experiments: TS, this study; Kess05a, Kessel *et al.* (2005*a*); Kess05b, Kessel *et al.* (2005*b*); Klimm08, Klimm *et al.* (2008); G&A03, Green & Adam (2003). Natural compositions: Dev94, Devey *et al.* (1994); Hoff88, Hofmann (1988); Kelley03, Kelley *et al.* (2003); LEG46-A3-Av: majors, Rb, Sr, Y, Zr, Nb: Dungan *et al.* (1979); Ti, V, Hf, Ta, Th: Bougault & Cambon (1979); Li, Sc, La, Ce, Nd, Sm, Eu, Dy, Lu: Emmermann & Puchelt (1979). Major element analyses are recalculated on an anhydrous basis for comparison; trace elements are given as published. —, either not reported or not added to the experiment; SD, standard deviation; Syn., synthetic; Av., average; Oc., oceanic; n.d., not determined; ∑LREE, SUM (La–Sm).

($Fe^{3+}/Fe^{tot} \approx 0{\cdot}3$–$0{\cdot}5$; $fO_2 >$ QFM), as well as some other elements (e.g. S, Rb) (e.g. Dungan *et al.*, 1979). Although carbon is also commonly enriched in basalts during sea-floor alteration, we do not find evidence for significant amounts of CO_2 in our selected samples (a carbonate phase would be expected at least in the sub-solidus experiment; e.g. Molina & Poli, 2000).

In Table 1, we compare the major and trace element composition of our starting materials with average MORB (Hofmann, 1988) and AOC (Kelley *et al.*, 2003), as well as with some other experimental starting materials with which we later compare our results. A significant contrast between the two starting material compositions is the low K_2O content of MORB [roughly comparable with that of Kessel *et al.* (2005*b*)] versus the order of magnitude higher K_2O content of AOC [roughly comparable with that reported by Green & Adam (2003) and Klimm *et al.* (2008)]. Other differences are marked by elevated Na_2O and TiO_2, as well as reduced MgO contents in the AOC sample.

Experimental techniques

Both starting materials were repeatedly ground with a mortar and pestle and then dried to produce a homogeneous powder. Distilled water (~1·8 μl) was injected into acid-cleaned and annealed Au ($T < 1000^{\circ}C$) or $Au_{80}Pd_{20}$ ($T \geq 1000^{\circ}C$) capsules using a Hamilton microsyringe (5 μl). Inaccuracies in injecting small quantities of water are compensated by adjusting the amount of rock powder that is added afterwards such that final H_2O contents were around 15 wt %. The capsules were welded shut using a PUK microwelder. The negligible heating of the welder ensures that H_2O is retained in the capsules, as verified by weighing the water-bearing capsules before and after welding. The experimental cell

consisted of inner spacers of crushable alumina, a graphite furnace, outer sleeve of salt and Pyrex, and a W_{95}/Re_5–W_{75}/Re_{25} (Type D), alumina-sheathed axial thermocouple. The friction coefficient for this assembly is 3% (McDade *et al.*, 2002). No account was taken of any pressure effect on thermocouple e.m.f. Experiments were run in ½ inch, end-loaded piston-cylinder apparatus at the University of Bristol using the 'hot-piston-in' method. Experiments were conducted at a pressure (*P*) of 3 GPa; experimental temperatures (*T*) ranged between 750 and 1000°C. The pressure was selected to lie close to the average depth of the Wadati–Benioff zone worldwide (≈105 km; Syracuse & Abers, 2006). Temperatures were selected to bracket the solidus and are in rough agreement with recent thermal models of slab-top temperatures beneath arcs (e.g. van Keken *et al.*, 2002; Syracuse *et al.*, 2010; Cooper *et al.*, 2012). Run durations were 2–7 days, in inverse proportion to temperature. Supra-liquidus runs were carried out at 1·5 GPa and ≥1325°C to produce glass from both starting materials for analysis. Runs were quenched by turning off the power.

One experiment was repeated at ETH Zürich after the original showed signs of disequilibrium (AOC 750°C run, lack of garnet). The same method and furnace assembly were used, but with a different thermocouple from that used at Bristol (Pt_{94}/Rh_6–Pt_{70}/Rh_{30}; Type B). Most importantly, this run was seeded with 2 wt % of gem quality garnet (composition ≈ $Py_{56}Alm_{37}Gross_1Spess_1Andr_5$; <7 μm fraction).

No attempt was made to control or monitor fO_2. Different pressure-cell assemblies can lead to variable fO_2 conditions in experiments (e.g. Truckenbrodt *et al.*, 1997), despite the use of a graphite furnace. For our assembly, in-house estimates of the fO_2 in Bristol lie in the range NNO + 2 (±1) (where NNO is nickel–nickel oxide buffer) for comparable *P*–*T*–time conditions. Conversely, if negligible water is lost to the assembly, and no iron is lost to the noble metal capsule, the fO_2 is simply a function of the initial Fe^{3+}/Fe^{tot} (e.g. Kagi *et al.*, 2005). In general, we find that the calculated ferric iron components in MORB and AOC runs are systematically different, which suggests that the fO_2 is at least partly controlled by initially different Fe^{2+}/Fe^{3+}. Because we cannot exclude that the initial fO_2 was modified during the experimental runs, we consider that the initial bulk Fe^{3+}/Fe^{tot} defines a lower fO_2 limit (∼QFM for MORB, >QFM for AOC; discussed above), and NNO + 2 (±1) an upper limit.

Analytical techniques

Carbon-coated, polished run products were imaged using a Hitachi S-3500N scanning electron microscope (SEM). Major element electron microprobe analysis (EMPA) was performed in Bristol on a five-spectrometer Cameca SX100 system, with 15 kV acceleration voltage and 15 nA sample current. The 750°C repeat experiment was measured at ETH on a five-spectrometer JEOL 8200 Superprobe, using similar conditions. A focused electron beam was used for minerals; for glasses, a defocused beam, and reduced sample current (4 nA) were used to reduce Na loss, with Na being counted first for 5 s only. Owing to size issues, a focused beam was applied for the quantification of 'fish egg' textured spherules (see below), which are also glassy in nature. These analyses thus probably are affected by loss of volatile elements such as Na_2O, and concomitant passive enrichment in other major elements.

Secondary ion mass spectrometry (SIMS) analysis of trace elements in experimental glasses was performed at the NERC facility at the University of Edinburgh using a Cameca IMS-4f ion microprobe. The following settings were applied: primary beam of 14·5 kV O^- ions; 5 nA beam current; ∼15 μm diameter beam. NIST SRM 610 glass (Pearce *et al.*, 1997) was used to calibrate relative ion yields; all data were ratioed to Si as determined by EMPA. A 75 ± 20 V energy filter was applied to positive secondary ions accelerated at 4·5 keV to reduce transmission of molecular ions. Subsurface inclusions were monitored in a count-rate versus time diagram and excluded from the averaging procedure. Molecular interferences were removed by conventional peak-stripping using in-house ION6 software. Matrix-dependent ion-yield differences between the calibrant (SRM 610) and natural glasses were evaluated by measuring different standards (MPI DING glasses: STHS, T1, ATHO; USGS glasses: GSD, BCR, BIR; standard values are taken from GeoRem: http://georem.mpch-mainz.gwdg.de) three times each over 4 days. Calculated Pearson correlation coefficients of calibration curves obtained from these standards are 0·97 or better (see Supplementary Data, file 1; supplementary data are available for downloading at http://www.petrology.oxfordjournals.org), despite the slope of the correlation being offset from unity, similar to what was found by Skora & Blundy (2012). The corrected bulk-rock data measured on the supra-solidus glasses agree well with trace element data given by Devey *et al.* (1994) for the MORB sample, and average Leg 46, 396B-#3A basalts for the AOC sample (Bougault & Cambon, 1979; Dungan *et al.*, 1979; Emmermann & Puchelt, 1979) (Table 1).

Trace elements in glasses from the repeat experiment (AOC 750°C) were measured by laser ablation inductively coupled plasma mass spectrometry (LA-ICP-MS) at ETH Zürich, using a Resonetics excimer laser (193 nm) coupled to a Thermo Element 2 ICP-MS system. The following settings were applied: spot size 30 μm; frequency 5 Hz; fluency 3·5 J cm^{-2}; acquisition time 30 s (blank) and 40 s (peak); standards were NIST SRM 612 (external), Ca (internal) and GSD-1G (secondary). Data were reduced using the Sills software (Guillong *et al.*, 2008), and mineral inclusions were excluded from the glass data via inspection of a count-rate versus time diagram.

To verify the consistency of the SIMS and LA-ICP-MS method we re-analysed all AOC experiments by

LA-ICP-MS. There is general agreement between both datasets to mostly better than ±20% except for elements with low overall abundances (<0·1 ppm). A comparison of SIMS and LA-ICP-MS analyses for the supra-liquidus runs is given in Supplementary Data file 1. In 800–900°C runs where melt segregation was incomplete the LA-ICP-MS technique encountered problems with numerous subsurface inclusions. We therefore prefer to report SIMS data wherever possible. Careful inspection of SIMS and LA-ICP-MS data further suggested a minor surface contamination of Ba from sample preparation. Owing to the vesicular nature of the glasses, surface contamination can penetrate into the uppermost few micrometres, which is beyond the sputtering depth of SIMS. For this reason we report LA-ICP-MS Ba concentrations instead, given that the latter method integrates the signal from a much greater depth (~20 μm).

RESULTS

Phase relations

All experiments but one (Bristol AOC run at 750°C, no garnet) produced an eclogitic residual assemblage (garnet, omphacitic clinopyroxene) along with some minor and accessory phases (e.g. kyanite, epidote, rutile, Fe–Ti oxide). Owing to the water-rich nature of these experiments, all run products contain abundant glass (quenched, supra-solidus melt) that often exhibits evidence for the presence of a coexisting vapour phase in the form of large vapour bubbles. These are sometimes decorated with 'fish egg' textured spherules, thought to represent the quenched silicate fraction of a vapour phase rich in dissolved silicates [see Adam *et al.* (1997); discussed below in more detail]. Melt–fluid segregation towards the top of the capsule occurred in most runs. All phase proportions (Fig. 1 and Table 2) were determined by least-squares regression for average compositions of major phases only, recalculated on an anhydrous basis. Water is reintegrated into the mass balance at a later stage (e.g. Klimm *et al.*, 2008). It should be noted that owing to the presence of two immiscible fluids (hydrous melt and siliceous vapour) we cannot calculate the H_2O content of the melt phase, because the fraction of the vapour phase is unconstrained. Thus the calculated liquid fraction in Table 2 represents the bulk liquid (melt + vapour), and not just the melt fraction.

Mineral textures and phase petrology vary slightly between MORB and AOC run products. Selected SEM images are given in Fig. 2. In general, MORB experiments at 800–900°C contain phases that tend to be relatively fine-grained (5–20 μm diameter). Garnets are inclusion-poor and chemically homogeneous when compared with many other experimental studies. At 1000°C, in contrast, garnets are relatively coarse grained (20–40 μm), inclusion-rich and zoned.

The sub-solidus MORB experiment (800°C) contains garnet, clinopyroxene, kyanite, epidote, quartz–coesite, rutile, and abundant vapour (no melt). Neither apatite nor phengite was observed owing to low bulk K_2O and P_2O_5 respectively (Table 1). Glass and additional garnet replace quartz–coesite, kyanite and some clinoyproxene in the 850°C experiment. Iron–Ti oxide also appears above the solidus. Importantly, epidote remains present above the solidus and does not change in composition to allanite [rare earth element (REE)-rich epidote-group mineral] as observed in the doped experiments of Klimm *et al.* (2008). Glasses at 850–900°C exhibit two distinct types of vesicles: microvesicles (approximately submicrometre to 1 μm) and large (~10–100 μm), irregular vesicles that may or may not contain 'fish eggs'. Microvesicles are common in quenched glasses in water-rich experiments (e.g. Klimm *et al.*, 2008) and are typically ascribed to the fact that the maximum amount of water that can be quenched into room temperature glasses is only 8–10 wt % (e.g. McMillan & Holloway, 1987), whereas the solubility of water in melts at run conditions is significantly higher (>35 wt % at $P \geq 4$ GPa; e.g. Kessel *et al.*, 2005*b*). The second, larger set of vesicles is thought to represent a siliceous vapour phase that coexisted with melt at run conditions, exsolving the silicate fraction upon quench to form 'fish eggs'. At 1000°C epidote and rutile melted out, but a variety of quench crystals (phengite and other, unidentified, very small phases) are present. In addition, there is no textural evidence for an additional vapour phase at 1000°C.

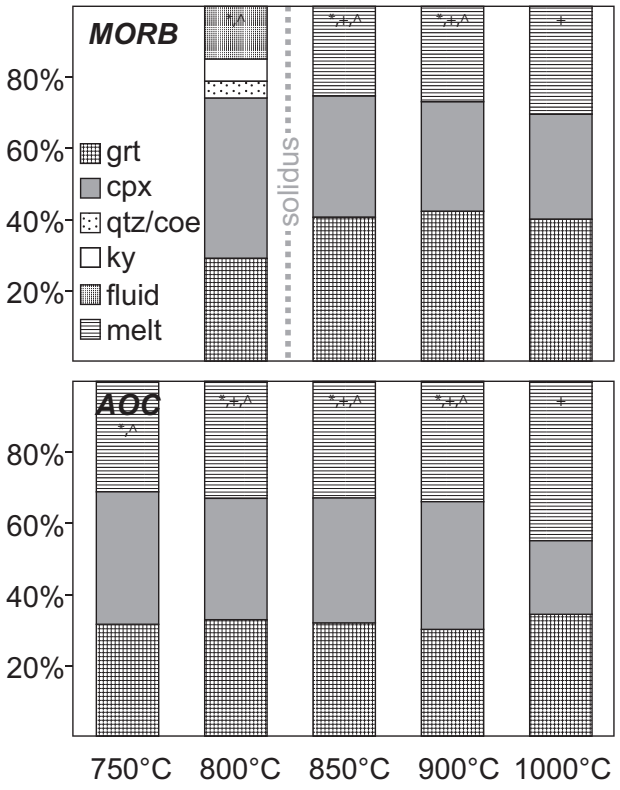

Fig. 1. Phase proportions in experiments on MORB and AOC (Table 2). grt, garnet; cpx, clinopyroxene; qtz/coe, quartz–coesite; ky, kyanite; *, trace epidote; +, trace Fe–Ti oxide; ^, trace rutile.

Table 2: Run conditions and phase proportions

Run	Time	*T*	Major phases (%)									
	(days)	(°C)	grt	cpx	qtz–coe	(st*)–ky	Fe–Ti	phen	liq	vapour	glass	trace phases
MORB												
LC2	7	800	29·1	44·9	4·7	6·2	—	—	15·0	X + FE	—	ep, rt
			34·3	*52·9*	*5·5*	*7·3*	—	—	—			
LC1	5	850	40·7	33·9	—	—	—	—	25·3	X + FE	X	ep, Fe–Ti, rt
			47·2	*39·5*	—	—	—	—	*13·3*			
LC3B	4	900	42·5	30·7	—	—	—	—	26·9	X	X	ep, Fe–Ti, rt
			49·2	*35·5*	—	—	—	—	*15·3*			
LC4	3	1000	40·7	29·3	—	—	—	—	30·2	—	X	Fe–Ti
			47·0	*33·8*	—	—	—	—	*19·4*			
AOC												
LCA0	8	750	—	59·6	5·9	15·9	1·7	1·8	15·0	X + FE	—	ep, rt, apa
			—	*70·2*	*7·0*	*18·7*	*2·1*	*2·1*	—			
LCA0 rep†	8	750	31·5	37·4	—	—	—	—	31·1	X	X	ep, rt, grt seeds
			36·3	*43·1*	—	—	—	—	*20·6*			
LCA2B	7	800	32·7	34·3	—	—	—	—	33·0	X + FE	X	ep, rt, Fe–Ti, ky
			37·6	*39·5*	—	—	—	—	*22·9*			
LCA1	5	850	31·8	35·4	—	—	—	—	32·7	(X)	X	ep, rt, Fe–Ti, ky
			36·6	*40·8*	—	—	—	—	*22·7*			
LCA3	4	900	30·3	35·7	—	—	—	—	34·0	—	X	ep, rt, Fe–Ti, ky
			34·8	*40·9*	—	—	—	—	*24·3*			
LCA4	3	1000	34·3	20·7	—	—	—	—	45·1	—	X	Fe–Ti
			38·8	*23·4*	—	—	—	—	37·8			

P = 3 GPa. grt, garnet; cpx, clinopyroxene; qtz–coe, quartz–coesite; ky, kyanite; Fe–Ti, Fe–Ti oxide; phen, phengite; liq, bulk liquid; ep, epidote; rt, rutile; apa, apatite; FE, 'fish eggs'; (st*) refers to the presence of staurolite as Al-rich phase in AOC sub-solidus experiment; X refers to the presence of vapour and/or glass; (X), presence of vapour is ambiguous in this run. Mass balances were initially performed using anhydrous compositions (values in italic), and H_2O was later reintegrated (see text).

†LCA0 rep is a repeat experiment of LCA0, run with grt seeds at ETH Zürich; further details are given in the Methods section.

Major phases in AOC run products at 800–1000°C are relatively coarse-grained (20–80 μm). Minor phases (e.g. rutile, etc.) are fine-grained (5–20 μm). The coarse-grained garnets are often inclusion-rich, and exhibit typical growth zoning. In contrast, the AOC 750°C repeat experiment exhibits many small garnets owing to the presence of garnet seeds in this run (Fig. 2). In clinopyroxenes, we find that omphacitic rims often overgrow smaller, Na-poor cores, which are probably magmatic relicts, given that their compositions are similar to those in the ODP report of Sato *et al.* (1979). Igneous clinopyroxenes apparently provided nuclei for high-pressure experimental clinopyroxenes. Fortunately, relict clinopyroxene cores in AOC experiments are of minor volumetric abundance compared with their omphacitic rims.

One AOC experiment (Bristol, 750°C) contains clinopyroxene, staurolite, phengite, epidote, quartz–coesite, rutile, Fe–Ti oxide, apatite and vapour with abundant 'fish eggs'. Garnet and clear evidence for melt are lacking. Repeating this experiment at ETH with garnet seeds produced abundant garnet, as growth rims (Fig. 2), clinopyroxene, glass and rutile, as well as fine-grained epidote–clinozoisite; we interpret this repeat run as a more close approach to equilibrium (see detailed discussion below). Changes in phase assemblages and proportions are fairly consistent with increasing temperature. Glass, garnet, clinopyroxene and some trace phases (rutile, Fe–Ti oxide, epidote, kyanite) remain present up to 900°C. Apatite is either melted out above the solidus or too small to observe. Similar to MORB experiments, a vesicular glass coexists with an additional fluid phase (large vesicles with or without fish eggs) at 750–850°C. The 900°C run product visually differs from the 850°C run product by having a slightly increased glass fraction and no clear evidence for the second fluid phase. At 1000°C glass, with quench crystals, is abundant (>40%), and epidote, rutile and kyanite are melted out.

Approach to equilibrium

It is straightforward to show that near-equilibrium conditions were reached with our MORB starting material, which was a glassy basalt with less than 10% olivine and minor plagioclase and spinel. All igneous phases were fully replaced by an eclogitic assemblage (garnet, clinopyroxene, other minor and accessory phases, as well as melt above the solidus), which is relatively homogeneous and comparable with the results of other studies (Supplementary Data file 2). The AOC run products exhibit broadly similar phase assemblages, as well as melt and mineral compositions that are comparable with MORB run products (Supplementary Data file 2). This suggests that near-equilibrium conditions were reached in all but a single Bristol AOC run at 750°C, which lacked garnet. The failure of garnet to nucleate can be explained by its sluggish nucleation kinetics in high-pressure experiments. This conclusion is consistent with the presence of garnet overgrowth rims in the garnet-seeded, repeat experiment at ETH Zürich, indicating that garnet belongs to the high-pressure sub-solidus assemblage at 3 GPa, 750°C. Other AOC run

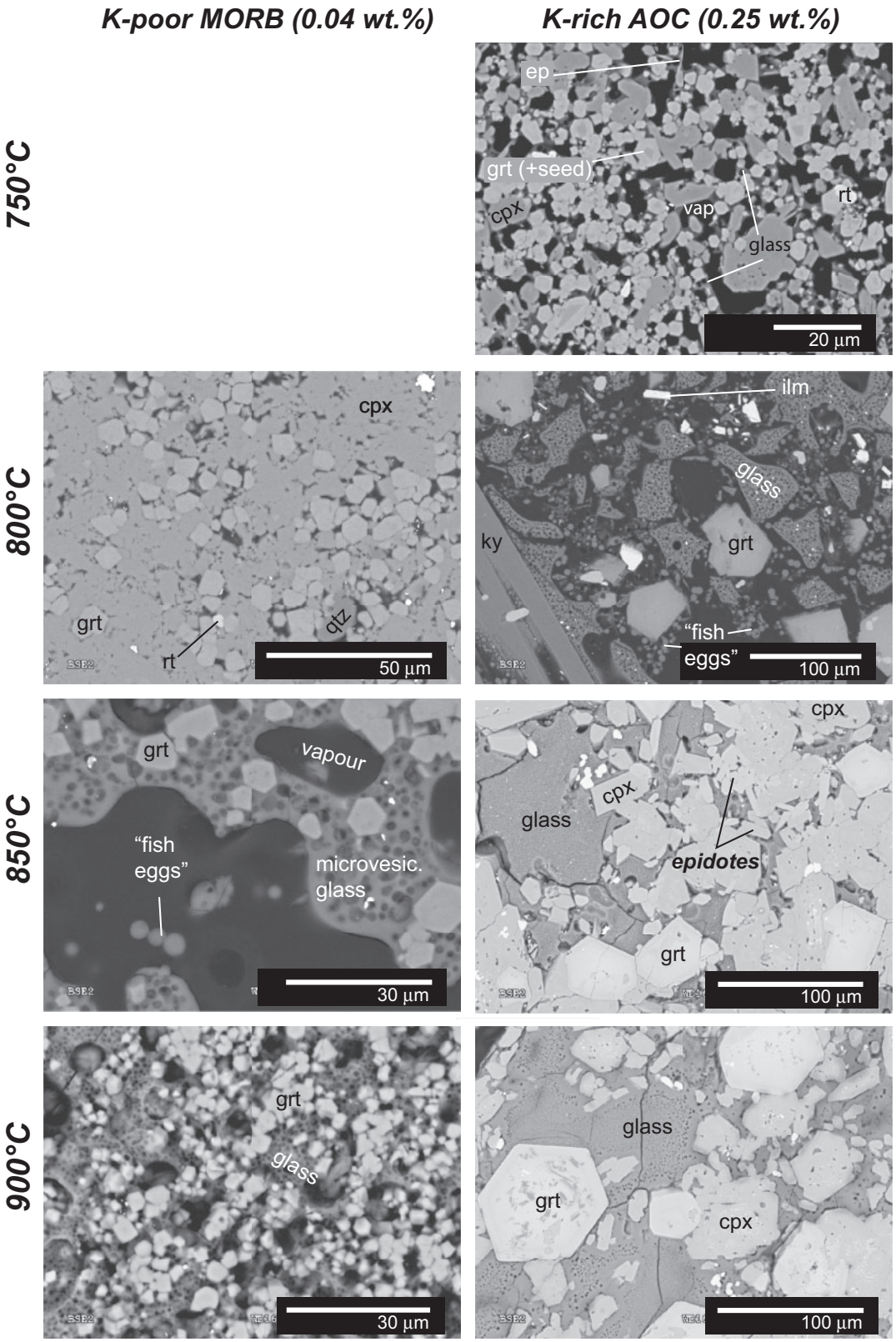

Fig. 2. Representative back-scattered electron (BSE) images of experimental run products at different temperatures in MORB and AOC. Mineral abbreviations as in Fig. 1; plus ilm, ilmenite; rt, rutile; vap, vapour; ep, epidote. Partial melts are always microvesicular owing to exsolution of water upon quench. In some experiments, we find clear evidence for the presence of a vapour phase in addition to glass, as evidenced by a second, larger generation of vesicles often containing 'fish egg' textured spherules [quenched silicate fraction of a fluid phase rich in dissolved silicates; see Adam *et al.* (1997)].

products also exhibit some features indicative of local disequilibrium, including growth zoning in garnet as well as small relict igneous clinopyroxenes that are surrounded by omphacite. Mass balance and all interpretations below are based on volumetrically dominant garnet and clinopyroxene rim compositions, because they will be in equilibrium with the coexisting phases.

Phase chemistry—major elements

Experimental glasses and silicate minerals are relatively homogeneous: in most cases major elements have 1σ of $<10\%$ relative; minor elements have $1\sigma = 10$–50% relative (Table 3). Notable exceptions are glasses in the MORB 850°C experiment, hampered because the small melt pools are not well interconnected, as well as both 1000°C experiments owing to the development of abundant quench crystals. In the latter cases, however, the average of a large number of analyses should approximate the equilibrium composition, despite large standard errors. Glasses are generally rich in SiO_2, Al_2O_3, CaO and alkalis, and poor in MgO and FeO. Low EMPA totals as well as the microvesicular nature of quenched glasses imply that they contain significant H_2O. 'Fish egg' textured spherules also appear glassy in nature and are broadly granitic in composition (see Table 4).

The MORB partial melts are peraluminous and tonalitic in composition [according to the classification scheme of Barker (1979)] just above the solidus, trending towards a more metaluminous composition at higher temperatures (Fig. 3). The AOC partial melts are also peraluminous, but trondhjemitic. Like MORB melts, they become metaluminous at higher temperatures, and further change their composition at $T \geq 900$°C to become tonalitic (Fig. 3). Magnesium oxide and FeO contents of all glasses are uniformly low, although both elements increase slightly at higher temperatures (Fig. 4). The Mg# decreases slightly between 750 and 1000°C from around 0·5–0·6 to around 0·4–0·5 in both experimental sequences (Table 3). Such compositions are fully consistent with other published studies on partial melts of a basaltic composition with excess water (range 5–25 wt %) at broadly similar *P*–*T* conditions [e.g. Ryabchikov *et al.*, 1996 (E3 composition); Prouteau

Table 3: Major and minor element compositions of experimental glasses

Exp.:	LC1	LC1	LC1	LC3B	LC3B	LC3B	LC4	LC4	LC4	LCA0 rep	LCA0 rep	LCA0 rep
Type:	measured	SD	anhydr.	measured	SD	anhydr.	measured	SD	anhydr.	measured	SD	anhydr.
T (°C):	850	850	850	900	900	900	1000	1000	1000	750	750	750
	MORB	MORB	MORB	MORB	MORB	MORB	MORB	MORB	MORB	AOC	AOC	AOC
n:	24	24	24	36	36	36	52	52	52	8	8	8
wt %												
SiO_2	60	4	76	57	2	74	54	3	71	58	3	73
TiO_2	0·19	0·03	0·24	0·25	0·04	0·32	0·29	0·08	0·38	0·12	0·02	0·15
Al_2O_3	11·9	0·8	15·0	11·5	0·7	14·8	12·6	0·8	16·4	12·8	0·7	16·2
FeO_{tot}	0·9	0·2	1·2	0·9	0·1	1·1	1·5	0·9	1·9	0·7	0·1	0·8
MgO	0·5	0·4	0·7	0·3	0·1	0·4	1	1	1	0·5	0·1	0·6
CaO	2·9	0·3	3·7	3·8	0·6	4·9	4	1	6	1·7	0·2	2·2
Na_2O	1·8	0·5	2·3	2·8	0·3	3·6	2·4	0·7	3·1	4·4	0·2	5·5
K_2O	0·4	0·2	0·5	0·7	0·2	0·9	0·5	0·3	0·7	0·9	0·1	1·1
P_2O_5	0·2	0·1	0·2	0·2	0·1	0·3	0·1	0·1	0·1	0·11	0·04	0·14
Sum	79	5	100	78	2	100	77	3	100	79	4	100
Al/(K + Na + 2Ca)	1·4	0·2	1·4	0·9	0·1	0·9	1·0	0·2	1·0	1·1	0·1	1·1
(Na + K)/Al	0·29	0·07	0·29	0·47	0·05	0·47	0·36	0·09	0·36	0·64	0·06	0·64
Mg#	0·5	0·4	0·5	0·4	0·2	0·4	0·5	0·8	0·5	0·6	0·2	0·6

Exp.:	LCA2B	LCA2B	LCA2B	LCA1	LCA1	LCA1	LCA3	LCA3	LCA3	LCA4	LCA4	LCA4
Type:	measured	SD	anhydr.	measured	SD	anhydr.	measured	SD	anhydr.	measured	SD	anhydr.
T (°C):	800	800	800	850	850	850	900	900	900	1000	1000	1000
	AOC	AOC	AOC	AOC	AOC	AOC	AOC	AOC	AOC	AOC	AOC	AOC
n:	46	46	46	34	34	34	36	36	36	44	44	44
wt %												
SiO_2	59	3	74	61	2	72	61	1	70	54	5	65
TiO_2	0·15	0·02	0·19	0·21	0·03	0·25	0·41	0·03	0·47	0·8	0·2	0·9
Al_2O_3	12·5	0·9	15·7	13·6	0·6	16·1	14·3	0·3	16·5	14	1	17
FeO_{tot}	0·8	0·1	1·0	0·9	0·2	1·1	1·6	0·1	1·8	3	1	3
MgO	0·6	0·2	0·8	0·3	0·2	0·4	0·9	0·1	1·0	1·3	0·8	1·5
CaO	1·9	0·2	2·4	2·3	0·3	2·7	3·9	0·3	4·5	6	3	8
Na_2O	2·8	0·4	3·6	4·6	0·5	5·4	3·8	0·6	4·3	3	1	4
K_2O	1·4	0·2	1·8	1·4	0·3	1·7	0·96	0·08	1·11	0·7	0·2	0·9
P_2O_5	0·31	0·08	0·39	0·32	0·07	0·38	0·36	0·06	0·42	0·2	0·1	0·3
Sum	80	4	100	84	2	100	86·7	0·9	100·0	84	4	100
Al/(K + Na + 2Ca)	1·3	0·1	1·3	1·0	0·1	1·0	1·0	0·1	1·0	0·8	0·2	0·8
(Na + K)/Al	0·50	0·07	0·50	0·67	0·08	0·67	0·51	0·07	0·51	0·4	0·1	0·4
Mg#	0·6	0·2	0·6	0·4	0·2	0·4	0·5	0·1	0·5	0·4	0·3	0·4

SD refers to 1σ of *n* (number) analyses; anhydr., anhydrous.

et al., 2001 (3 GPa subset); Kessel *et al.*, 2005*b* (4 GPa, 900–1000°C subset); Klimm *et al.*, 2008; Prouteau & Scaillet, 2013] (Supplementary Data file 2). Remaining small discrepancies between all these studies can be related to differences in bulk composition, fO_2, pressure (range 2·5–4 GPa) and the degree of melting as a consequence of different starting H_2O contents.

Major element compositions of minerals are given in Supplementary Data file 3. The method of Droop (1987) was used to estimate Fe^{3+} contents for garnet and clinopyroxene and stoichiometric considerations are used for all other minerals. Garnets in MORB and AOC run products are compositionally similar at similar temperatures, being rich in almandine (25–40%), pyrope (30–44%) and grossular (23–30%), but poor in spessartine (<1%) and andradite (1–6%). Where zoning occurs, garnets display increasing pyrope and decreasing almandine from core to rim. A small but noticeable difference between the experimental sequences lies in the calculated andradite component, which tends to be lower at lower temperatures (800–900°C) in MORB (1–2·7%) than in AOC (1·7–6·5%), in keeping with higher initial Fe^{3+}/Fe^{tot} in AOC. In contrast, calculated andradite components are consistently higher (5·2–7·5%) at 1000°C. With increasing temperature, the pyrope component increases mostly at the expense of almandine, gradually changing the Mg# from around 0·4 to around 0·6. Garnet Mg# hence mirrors the behaviour of melts, which become more iron-rich at higher temperatures. Other minor elements observed in garnet include TiO_2, which increases slightly with increasing temperature in the presence of rutile. Experimental garnet compositions and chemical trends with temperature are fully consistent with other experimental studies (see Supplementary Data file 2).

Clinopyroxenes are all omphacites, and are less chemically variable than garnet. A comparison with other studies is given in Supplementary Data file 2. They exhibit a significant 'quadrilateral' (QUAD) Ca–Mg–Fe component (74–76% in MORB, 62–66% in AOC), a jadeite component (18–24% in MORB, 23–31% in AOC), and a small, but significant, calculated acmite component (2–8% in MORB, 3–11% in AOC). The acmite component is probably a maximum estimate owing to the possible presence of a small Ca-eskolaite component (e.g. Konzett *et al.*, 2007). The relict igneous cores in AOC (750–900°C) are ~90% QUAD in composition, with a relatively high acmite component (4·5–7·5%), and significantly higher Ti compared with high-pressure, omphacite rims.

Minor phases that were observed include kyanite, which is relatively pure Al_2SiO_5, although a small quantity of iron (probably Fe_2O_3) is detectable (~3 wt % in MORB; ~4 wt % in AOC). Epidotes are epidote–clinozoisite solid solutions, containing ~8–10 wt % total iron, which should be mostly Fe_2O_3. The SiO_2 phase that occurs in sub-solidus runs should be coesite, although this is hard to distinguish from quartz in our run products, based on textural criteria alone. Iron–Ti oxides of the ilmenite–hematite solid solution series are present in almost all runs, displaying a significant hematite component (~55–75 mol %), and a small Al_2O_3 component (~1–4 mol %). Rutile, which contains some ferric iron (~2–7 mol %), is present in all runs below 1000°C. Apatite was found in a single run only (750°C;

Table 4: Major and minor element composition of 'fish eggs'

Exp.:	LC1	LC1	LC1	LCA2B	LCA2B	LCA2B
Type:	measured	SD	anhydr.	measured	SD	anhydr.
T (°C):	850	850	850	800	800	800
	MORB	MORB	MORB	AOC	AOC	AOC
n:	7	7	7	13	13	13
wt %						
SiO_2	65	5	81	65	2	78
TiO_2	0·15	0·07	0·19	0·11	0·04	0·13
Al_2O_3	11	1	13	13	1	15
FeO_{tot}	0·7	0·3	0·8	0·4	0·1	0·5
MgO	0·4	0·2	0·5	0·4	0·3	0·4
CaO	2·5	0·4	3·1	1·8	0·4	2·2
Na_2O	0·5	0·3	0·6	1·6	0·5	1·9
K_2O	0·31	0·03	0·39	1·2	0·3	1·4
P_2O_5	0·05	0·03	0·06	0·15	0·05	0·18
Sum	80	6	100	83	2	100

SD refers to 1σ of *n* (number) analyses; anhydr., anhydrous.

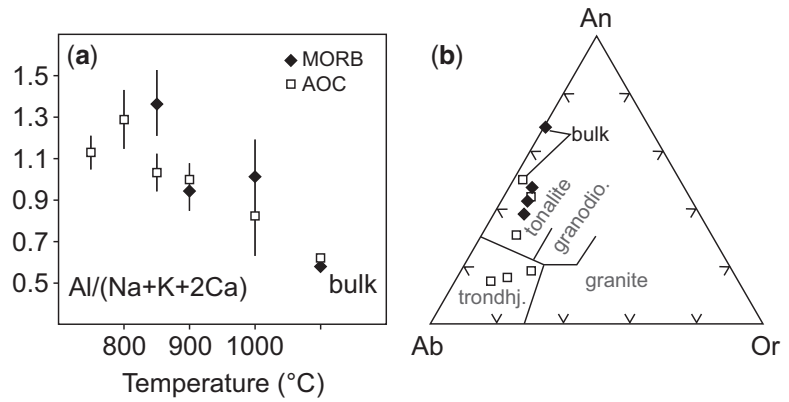

Fig. 3. (a) Al/(Na + K + 2Ca) ratios of quenched glasses showing a trend from peraluminous to metaluminous compositions at higher temperatures. (b) The granite classification scheme of Barker (1979), indicating that the experimental partial melts are trondhjemitic to tonalitic in composition.

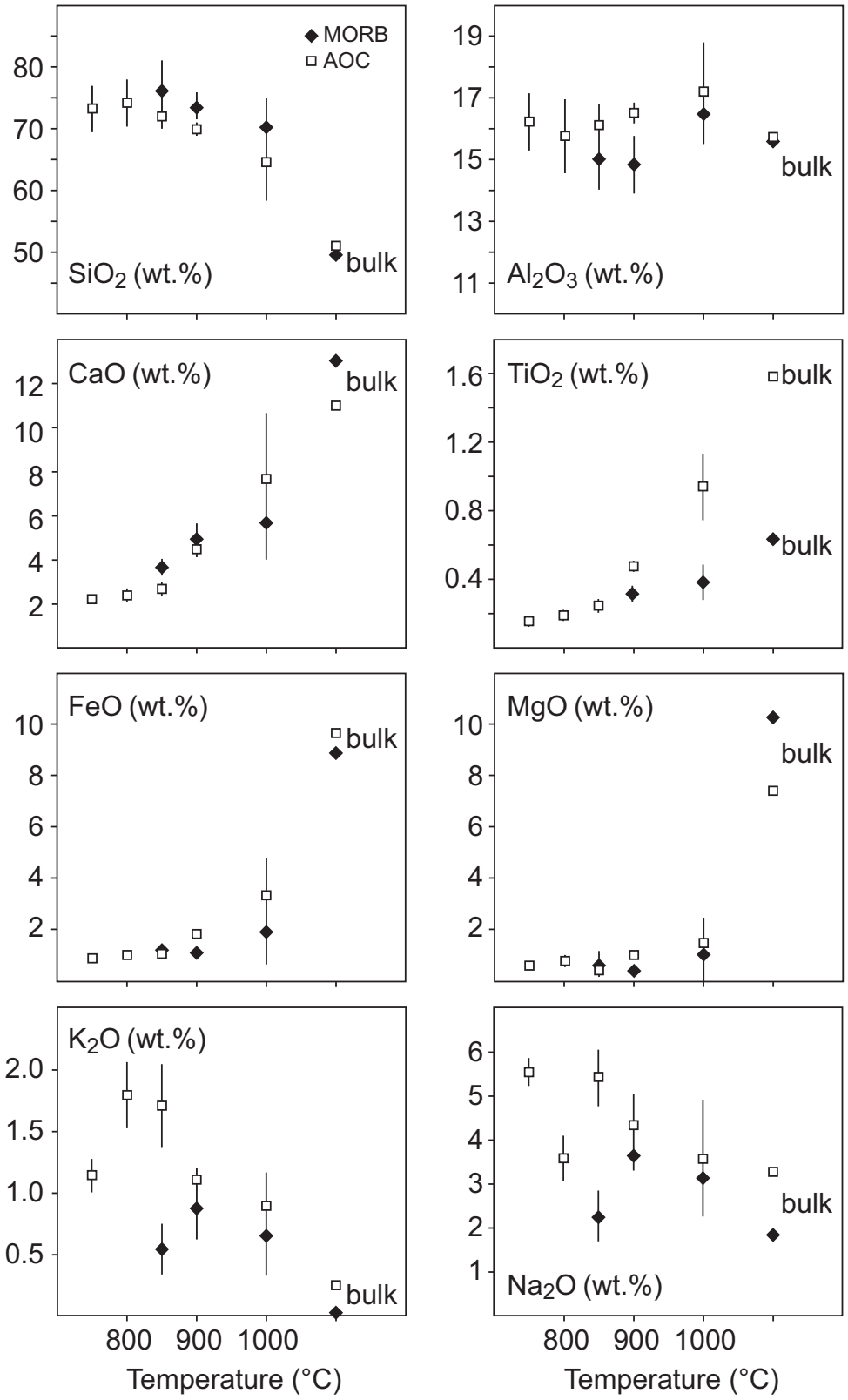

Fig. 4. Major element chemistry of quenched glasses (on an anhydrous basis) showing systematic changes with temperature. Where SiO_2 decreases, Al_2O_3 systematically increases with increasing temperature. The general tendency for CaO to increase with increasing temperature is consistent with the progressive consumption of clinopyroxene and epidote during melting. Titanium oxide contents increase systematically with increasing temperature in the presence of rutile because of increasing solubility.

Table 5: Trace element compositions of hydrous glasses

Exp.:	LC3B	LC3B	LC4	LC4	LCA0*	LCA0*	LCA2B	LCA2B	LCA1	LCA1	LCA3	LCA3	LCA4	LCA4
Type:	meas	SD	meas	SD	rep meas	rep SD	meas	SD	meas	SD	meas	SD	meas	SD
T (°C):	900	900	1000	1000	750	750	800	800	850	850	900	900	1000	1000
	MORB	MORB	MORB	MORB	AOC	AOC	AOC	AOC	AOC	AOC	AOC	AOC	AOC	AOC
n:	7	7	5	5	11	11	5	5	5	5	5	5	6	6
ppm														
Li	5·1	0·8	9	2	—	—	38	7	63	9	65	3	58	6
Sc	5·6	0·4	10	2	1·9	0·3	3·4	0·3	1·9	0·2	4·4	0·6	10·3	0·6
Ti	1770	50	3040	420	655	31	1020	150	1270	140	2580	60	7000	340
V	530	40	600	150	131	9	260	20	230	20	209	5	310	30
Rb	10	2	6	1	16·7	0·9	26	4	23	2	20	4	12	1
Sr	220	10	180	60	415	12	440	20	470	10	720	30	400	20
Y	1·9	0·2	2·9	0·9	0·60	0·05	3·0	0·4	0·75	0·06	1·9	0·1	7·4	0·4
Zr	40·3	0·9	56	5	43	2	81	6	96	3	181	5	151	4
Nb	2·2	0·1	4·4	0·3	0·24	0·03	0·50	0·09	0·49	0·06	0·92	0·06	4·8	0·2
Cs	0·4	0·1	0·4	0·1	3·4	0·2	1·6	0·2	1·6	0·7	1·3	0·2	0·6	0·2
Ba	—	—	—	—	18·4	0·8	23·3	0·9	27	1	20·7	0·8	19	4
La	0·52	0·06	1·6	0·8	<0·04	—	0·34	0·08	0·09	0·02	0·28	0·07	6·7	0·6
Ce	1·1	0·3	4	2	0·08	0·02	1·1	0·1	0·09	0·01	0·9	0·1	20	2
Nd	0·8	0·2	3	2	<0·02	—	0·8	0·1	0·09	0·06	1·2	0·2	15	2
Sm	0·24	0·08	1·0	0·6	<0·02	—	0·28	0·03	0·05	0·02	0·4	0·1	3·4	0·3
Eu	0·10	0·04	0·3	0·2	<0·06	—	0·12	0·06	0·05	0·04	0·16	0·03	0·89	0·05
Gd	0·21	0·03	0·7	0·3	<0·03	—	0·26	0·04	0·05	0·02	0·32	0·07	2·3	0·2
Dy	0·32	0·06	0·5	0·3	0·08	0·02	0·5	0·1	0·09	0·03	0·28	0·06	1·4	0·2
Lu	0·014	0·006	0·04	0·01	<0·02	—	0·022	0·004	b.d.l.	b.d.l.	0·011	0·004	0·10	0·02
Hf	0·9	0·2	1·5	0·2	1·6	0·2	2·4	0·2	2·8	0·3	5·1	0·4	3·7	0·3
Ta	0·08	0·01	0·22	0·05	<0·03	—	0·04	0·01	0·03	0·02	0·05	0·01	0·27	0·05
Th	0·11	0·04	0·27	0·08	<0·02	—	0·012	0·005	0·012	0·003	0·036	0·003	0·28	0·04
U	0·07	0·02	0·12	0·06	0·04	0·01	0·07	0·02	0·08	0·04	0·17	0·04	0·14	0·04
∑LREE	2·6	0·4	10	3	<0·2	—	2·5	0·2	0·3	0·1	2·7	0·2	45	2
Ba/Th	460	180	130	40	>920	—	1870	770	2330	610	580	50	70	20
La/Sm_{PUM}	1·5	0·3	1·1	0·5	—	—	0·8	0·1	1·3	0·5	0·4	0·1	1·3	0·1
U/Th_n	2	1	1·0	0·8	>3·5	—	10	6	12	9	9	4	0·9	0·4

*Experiment analyzed by LA-ICP-MS, all other experiments were analyzed by SIMS; Ba concentrations for AOC are LA-ICP-MS data; further details are given in the Methods section. Meas, measured; SD, 1 sigma standard deviation.

∑LREE = SUM (La–Sm); La/Sm_{PUM} are PUM normalized; U/Th_n are source normalized; b.d.l., below detection limit.

AOC without melt and garnet), suggesting that this is the main phase that carries P_2O_5 down to sub-arc depth in phosphate-rich basalts, until it is melted out above the solidus.

Glass chemistry—trace elements

With increasing temperature several systematic variations in glass chemistry are observed. Concentrations are given in Table 5 and plotted [normalized to primitive upper mantle (PUM)] in Fig. 5 and against temperature in Fig. 6. The AOC experiments provide the most complete dataset in terms of temperature evolution (750–1000°C), but some insights can also be derived from the MORB data at 900 and 1000°C. In general, fluid-mobile elements such as Cs, Rb, Ba, Sr and Li are always enriched in the partial melts. Other elements such as U, Zr, Hf, and V are also moderately enriched. Elements such as Nb, Ta, the light REE (LREE) and Th are relatively depleted at $T \leq 900$°C. Heavy REE (HREE), Y and Sc are relatively depleted at all temperatures. Different element groups behave differently with increasing temperature; for example, HREE, Y and Sc concentrations increase with increasing temperature, in contrast to most fluid-mobile elements. The different trace element patterns are explained in more detail below.

DISCUSSION

Location of the solidus

Our experiments place constraints on the 3 GPa, H_2O-saturated solidus of ocean floor basalt, which is shown to be sensitive to bulk K_2O content. Our AOC experiments (~0·25 wt % K_2O) produced glass (+ garnet, clinopyroxene, minor phases) at 750°C only in the experiment that contained garnet seeds. The other experiment at 750°C contained 'fish eggs' instead of melt, together with clinopyroxene, staurolite [for reasons detailed by Skora & Blundy (2010) staurolite is probably metastable relative to garnet and kyanite], phengite, quartz–coesite and minor phases. It is tempting to conclude that the lack of melt in the latter 750°C experiment is due to garnet nucleation problems and related overall disequilibrium. However, the most widely proposed H_2O-saturated melting reaction for K-bearing MORB and sediment is quartz–coesite + phengite + clinopyroxene + H_2O = melt + garnet (e.g. Schmidt, 1996; Hermann & Green, 2001; Hermann & Spandler, 2008; Skora & Blundy, 2010). As garnet is a product of melting, it is unlikely that the lack of garnet should inhibit melting. Alternatively, melting in K-bearing AOC may start at temperatures that are very close to 750°C, and small calibration-related *P–T* discrepancies between

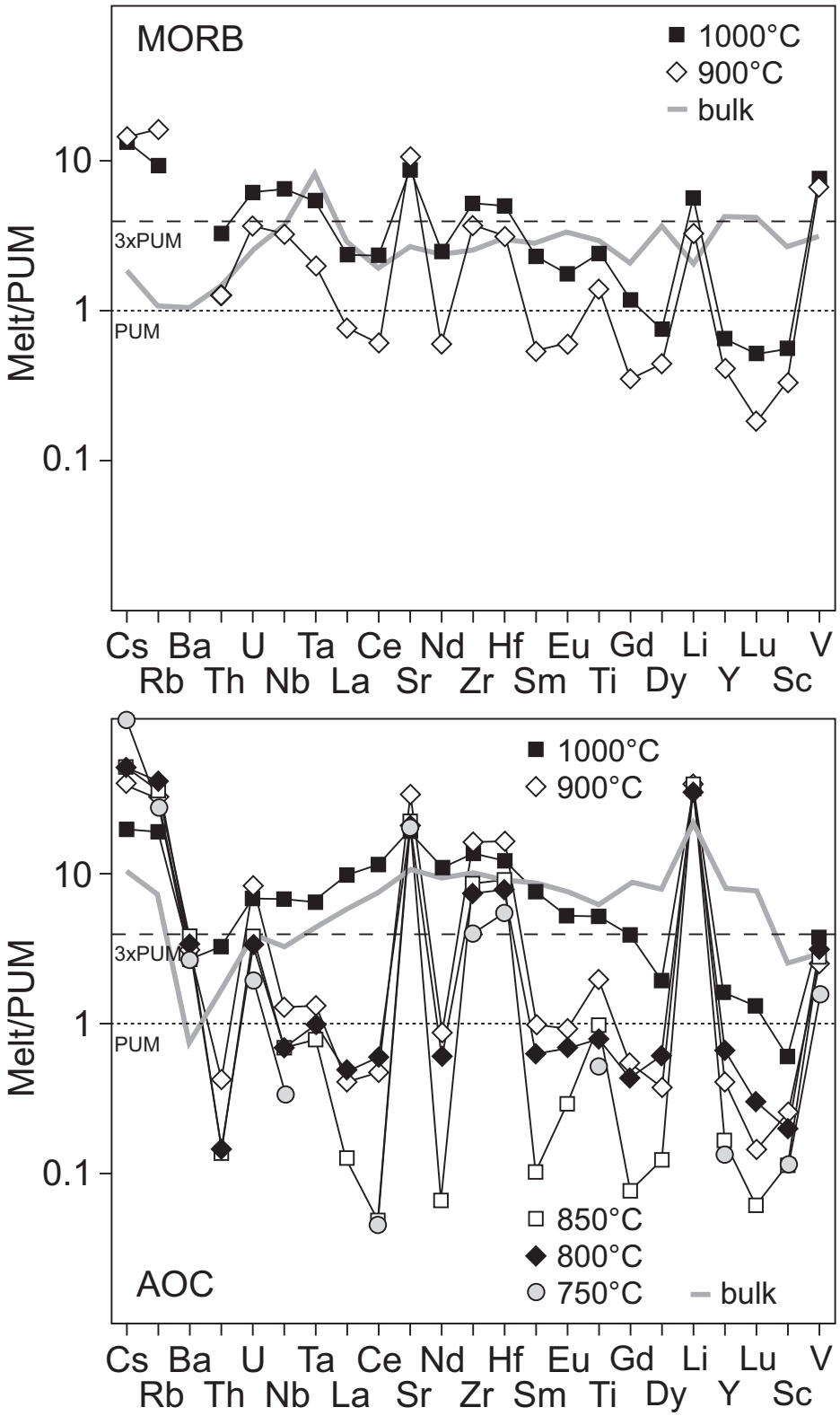

Fig. 5. Trace element compositions of experimental glasses normalized to PUM (primitive upper mantle; Sun & McDonough, 1989). Starting compositions are shown as thick continuous grey lines. At low temperatures trace element patterns are spiky, becoming smoother and approaching their levels in the starting materials as temperature increases. Fluid-mobile elements (e.g. alkalis) are the most enriched at all conditions. LREE are strongly depleted in partial melts, owing to the presence of residual epidote up to ~900°C. Glasses also show enrichment of Zr (over Nd), Hf (over Sm) and Li (over Y), although these characteristics are rarely reflected in arc magmas because of the subsequent control exerted by mantle wedge peridotite.

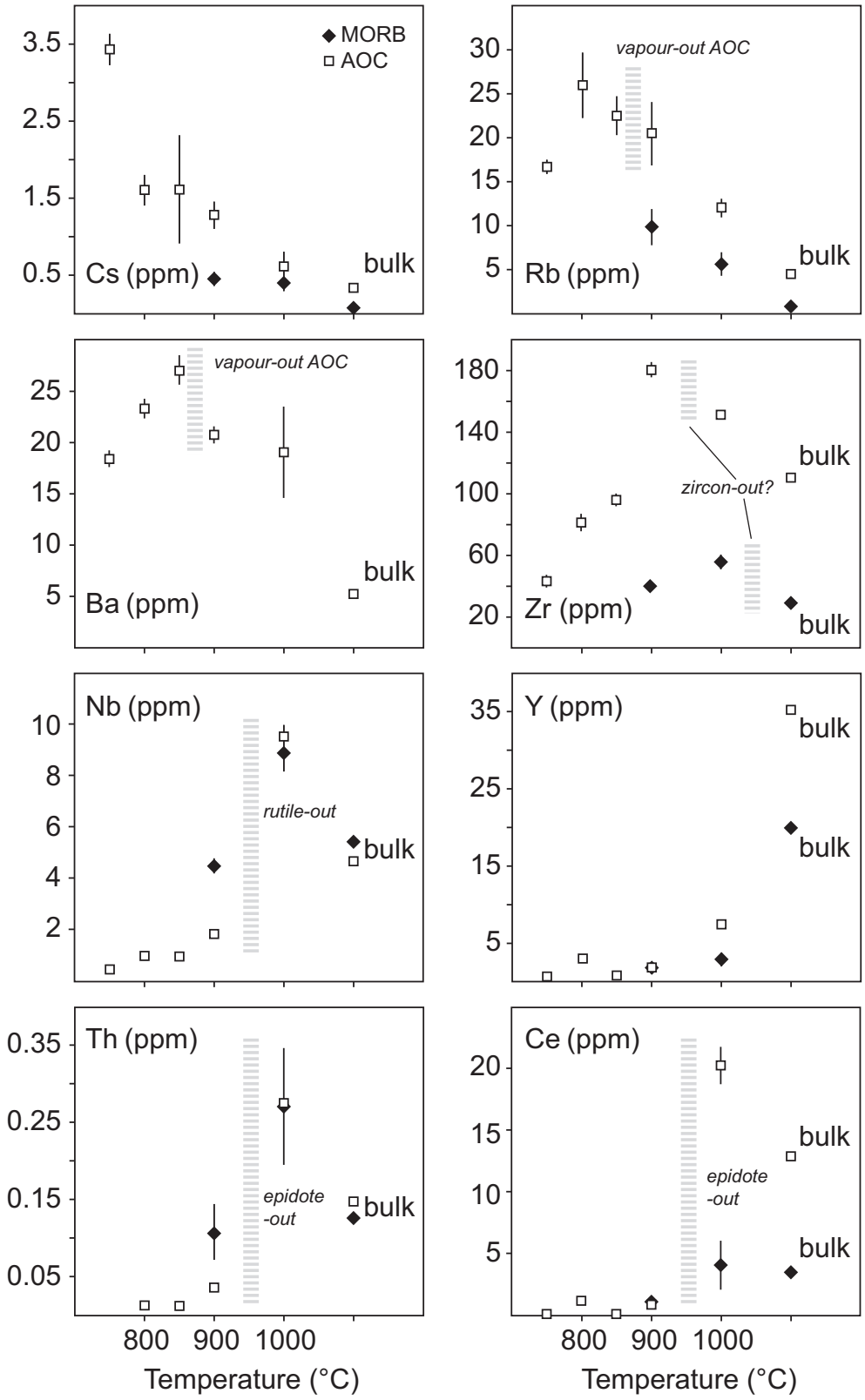

Fig. 6. Trace element chemistry of quenched glasses showing systematic changes with temperature. Different element groups behave differently with increasing temperature; for example, HREE, Y and Sc concentrations increase with increasing temperature, in contrast to most fluid-mobile elements. The different trace element patterns can be related to the presence or absence of residual phases as well as the additional vapour phase.

Bristol and ETH Zürich (e.g. owing to different thermocouple types) may be responsible. For basalt with 0·14 wt % K_2O and excess water, Lambert & Wyllie (1972) determined a 3 GPa solidus temperature of ~750°C, whereas Schmidt & Poli (1998) located their solidus at ~730°C for MORB with 0·49 wt % K_2O. Thus, regardless of whether the lack of melt in one 750°C experiment is due to *P–T* uncertainties or due to disequilibrium, we conclude that melting in K-rich AOC starts at $T \approx 750$°C, in keeping with previous studies.

Quenched silicate melt formed only above 800°C in the MORB experiments, placing the 3 GPa solidus for a starting material with only 0·04 wt % K_2O between 800 and 850°C ($T = 825 \pm 25$°C). In theory, no phase other than phengite is capable of hosting appreciable potassium in an eclogitic assemblage at around 3 GPa, a fact confirmed by analyses of silicate minerals in this run (Supplementary Data file 3). Sub-solidus phengite, however, was not observed. Possibly phengites were never found because 0·04 wt % initial K_2O equates to just ~0·4 vol % phengite. Alternatively appreciable potassium was dissolved in the siliceous fluid (quenched as 'fish eggs') at near-solidus conditions (Table 4), effectively stripping out all the potassium from the solid assemblage. We note that the K-free, water-rich experiments of Kessel *et al.* (2005*b*) determined a 4 GPa solidus temperature of 875 ± 12°C. Assuming a constant offset between K-bearing and K-free MORB at 3 and 4 GPa, the solidus estimates of Lambert & Wyllie (1972) and Kessel *et al.* (2005*b*) can be extrapolated to a 3 GPa, K-free MORB solidus temperature of around 850°C, consistent with our experimental results. The melting reaction, however, differs slightly from that given by Kessel *et al.* (2005*b*). We find that glass and garnet replace quartz–coesite, kyanite and some clinopyroxene in the 850°C experiment, suggesting an initially incongruent melting reaction of the form quartz–coesite + kyanite + clinopyroxene + H_2O = melt + garnet. Kessel *et al.* (2005*b*) proposed instead a congruent melting reaction of the form clinopyroxene + garnet = melt. To what extent the discrepancies relate to differences in pressure or bulk-rock composition remains uncertain at this stage, but it is evident that both reactions would occur at somewhat similar temperatures in subduction zones.

The question persists as to whether AOC and MORB can melt at Wadati–Benioff zone depths (~75–135 km, average ≈105 km; Syracuse *et al.*, 2010), provided that sufficient H_2O can be added via the breakdown of hydrous minerals such as serpentine or chlorite in deeper portions of the slab. Recent results in thermal modelling (e.g. Syracuse *et al.*, 2010; van Keken *et al.*, 2011) predict slab-top temperatures of around 750–850°C in most subduction zones at 2·5–4·5 GPa (e.g. Lesser Antilles), with some offset towards higher temperatures (850–950°C; e.g. Nicaragua, Guatemala). These temperatures drop off in the lower parts of the subducted column, and are ~100–300°C lower than slab-top temperatures at the bottom of a 7 km thick basaltic crust (e.g. van Keken *et al.*, 2011). Combined with our experimentally derived, H_2O-saturated solidus temperatures, these results suggest that only the top part of the basaltic crust can melt, if present as altered oceanic crust with elevated K_2O contents. K-poor MORB is less likely to melt except in the hottest subduction zones. Melt fractions of oceanic basalts will be significantly lower compared with those of overlying, K-rich marine sediments (e.g. Schmidt *et al.*, 2004).

Nature of experimental fluids

The second critical end-point (SCEP) is defined in *P–T* space by the intersection of the melt–vapour critical curve and the H_2O-saturated solidus (see, e.g. Manning, 2004; Hermann *et al.*, 2006). The conventional designation of solidus, melt and vapour is lost at pressures exceeding the SCEP because melt and H_2O are fully miscible supercritical fluids. Experimental studies have come to different conclusions concerning the position of the SCEP in the system basalt–H_2O (or more correctly the system basalt-derived partial melt–H_2O). Kessel *et al.* (2005*b*) used topological criteria to estimate the SCEP in K-free basalt to lie between 5 and 6 GPa. This is close to the position of the SCEP in K-MORB as estimated by Schmidt *et al.* (2004) using textural evidence. On the basis of extrapolation from the haplogranite critical curve to the H_2O-saturated basalt solidus, Klimm *et al.* (2008) proposed that the SCEP lies at ~2·5 GPa in K-MORB. This discrepancy raises the question of whether MORB- or AOC-derived fluids beneath arcs are supercritical in nature, or not.

In our experimental charges, MORB glasses at 850–900°C and AOC glasses at 800–850°C clearly exhibit two distinct types of vesicles: (1) microvesicles that are evident in all glass pools; (2) large, irregular vesicles that are also present in glass pools and that may or may not contain 'fish eggs'. Microvesicles in glasses (1) are commonly interpreted to represent vapour-exsolution upon quench (e.g. Klimm *et al.*, 2008). Larger vesicles (2) are interpreted to represent an additional vapour phase that coexisted with hydrous melt (= quenched glasses) at run conditions. The 'fish eggs' are suggested to represent the siliceous fraction that was dissolved in the vapour phase at run conditions. Our textural evidence argues for two fluid phases at near-solidus conditions, hydrous melt + siliceous vapour (Fig. 7). Our experimental data thus suggest sub-critical conditions and place the SCEP at pressures greater than 3 GPa in both MORB- and AOC-derived fluids, consistent with Schmidt *et al.* (2004) and Kessel *et al.* (2005*b*). Above 900°C (MORB) and 850°C (AOC), clear evidence for an additional vapour phase (± 'fish egg' textured spherules) disappears, suggesting that complete fluid–melt miscibility (supercritical behaviour) may occur in response to increasing temperature and changing melt composition. We further offer a possible explanation for the discrepant result of Klimm *et al.* (2008) in Supplementary Data file 4.

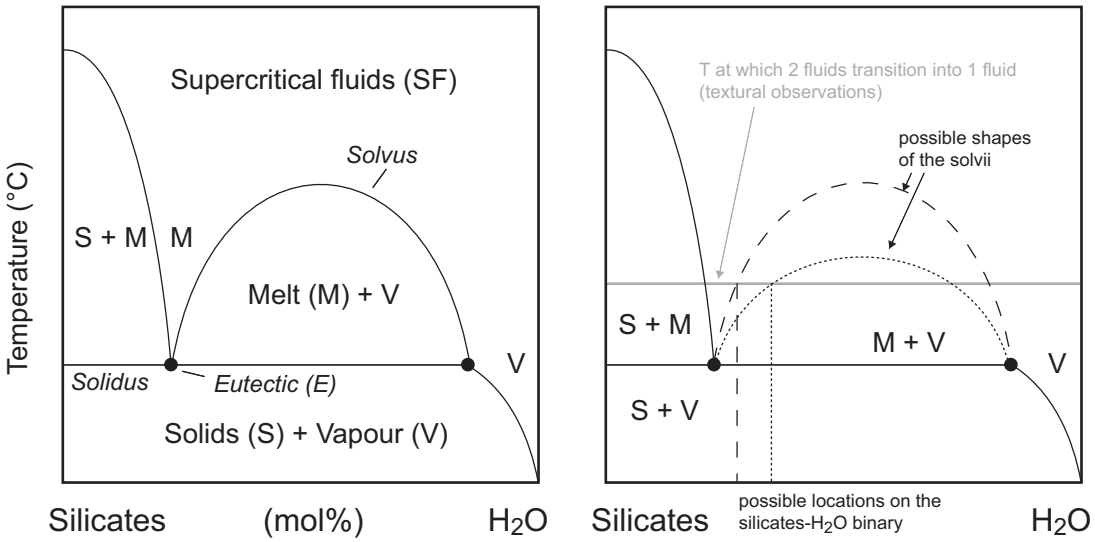

Fig. 7. Schematic subcritical silicate–H_2O diagram versus temperature at constant pressure (3 GPa) (after Manning, 2004). It should be noted that this sketch does not attempt to illustrate the chemography of our bulk-rocks. Instead, the sketch approximates melt–fluid equilibrium in a simplified case in which the bulk composition corresponds to the minimum melt (+ H_2O) of AOC and MORB. Different residual solid phases that are present in our experimental run products are ignored here. It is illustrated in the right panel that our experiments constrain only the temperature at which two fluids condense to a single fluid (solvus: dashed lines). However, the position along the abscissa is not constrained because we did not vary the experimental water content. It is therefore possible that two fluids would have been present at higher temperatures, had more water been added.

Trace elements in fluid and melt

It is well known that the behaviour of trace and minor elements in the glass with increasing temperature is a direct consequence of the residual mineralogy, specifically the phases that control the budget of those elements (e.g. rutile; Klemme *et al.*, 2002). For elements that lack a residual host phase the concentration in the glass will decrease with temperature, whereas for elements with a ubiquitous host phase, element concentrations will increase with temperature. For elements whose host phase becomes exhausted over the melting interval the concentration in the glass will attain a maximum at the point of phase exhaustion. Naturally all trace element contents attain those of the bulk starting material at the liquidus temperature. A complexity arises for those elements that strongly partition into a separate vapour phase; that is, for sub-critical conditions. In that case the exhaustion of the vapour phase upon attainment of criticality will lead to a maximum in glass concentration in much the same way as exhaustion of a solid residual phase.

Titanium, Nb and Ta show a continuous increase in concentration with temperature, with the same trends observed for MORB and AOC, consistent with the persistence of residual rutile up to 900°C and Fe–Ti-oxide thereafter (Fig. 6). It should be noted that Fe–Ti oxides are unlikely to host significant quantities of Nb and Ta because of the significant hematite component (see Skora & Blundy, 2010). In AOC glasses Zr (and Hf) shows a marked peak in concentration at around 900°C (Fig. 6). We lack the resolution in MORB glasses to establish if there is a maximum or not. The tendency of Zr and Hf to attain maxima at intermediate temperatures in AOC suggests the exhaustion of zircon at ~900°C during melting, although zircon was never positively identified in our experiments owing to low bulk Zr. Scandium, V, Y and HREE also show an overall increase in the glass from 750 to 1000°C owing to the persistence of garnet and, to a lesser extent, omphacite across the melting interval (Fig. 6). The slightly complex behaviour of Sc and V may reflect competition between garnet and omphacite and their changing proportion in the residue with increasing temperature. LREE abundances are extremely low (<1–3 ppm total LREE) in all glass-bearing experiments on MORB and AOC, except at the highest temperature when their concentrations increase sharply (Fig. 6). This behaviour is a consequence of residual epidote, which is known to host these elements (e.g. Frei *et al.*, 2004) and approaches exhaustion at the highest run temperatures. The 800°C AOC run has higher LREE than either of the adjacent runs. This behaviour is suggestive of less epidote in this run, which may be a result of a small inter-run variability in fO_2, which influences epidote stability and proportion through control of Fe^{3+}. Uranium and Th concentrations are also very low (<0·3 ppm) in all experimental glasses, and consequently subject to high analytical uncertainty, making trends hard to discern. Nonetheless Th clearly increases with temperature until $T = 900$°C, similar to Ce (Fig. 6). Again, epidote appears responsible for this behaviour.

The large ion lithophile elements (LILE) K, Ba, Cs, Rb, Sr and Li in glasses show variable behaviour (Fig. 6). Caesium decreases steadily with temperature in the AOC and MORB experiments, indicative of behaviour as an incompatible element with no residual host phase.

Potassium and Rb show broad maxima at around 800–850°C in AOC, and 900°C (K only) in MORB. Barium in AOC shows a maximum at 850°C, whereas Li shows a broad maximum at 850–900°C. Strontium shows a maximum between 900 and 1000°C in both sets of experiments. Finally, Na shows a maximum in MORB at 900°C, but rather irregular behaviour in AOC. With the possible exceptions of Sr in epidote (Supplementary Data file 5) and Na and Li in omphacite (e.g. Hermann 2002*a*), none of the LILE have a residual host phase; phengite, a potential host for K and Ba, is exhausted above the solidus of MORB and AOC. Thus the maxima that the LILE display cannot be ascribed to exhaustion of a solid phase. However, it is striking that the various maxima displayed by LILE roughly correspond to the transition from sub-critical to super-critical behaviour (850–900°C in AOC, 900–1000°C in MORB), as evidenced texturally, suggesting a role for fluids in LILE transport. In much the same way as exhaustion of a solid phase produces maxima for other trace elements so the exhaustion of the fluid phase on crossing the solvus into super-critical behaviour can lead to maxima in the concentrations of elements that possibly partition into the fluid. In detail, the temperature at which the maximum occurs over the transition to supercritical behaviour will reflect the strength of partitioning into the fluid. Thus our data suggest that fluid–melt partitioning increases in the order Cs < Rb < K < Ba in AOC. The behaviour of Na in this sequence is unclear. This is an interesting insight into LILE fluid partitioning, but dedicated experiments would be required to quantify it.

Allanite versus epidote and the behaviour of LREE

The behaviour of LREE + Th in our experimental glasses is controlled by the presence of residual epidote. LREE abundances are extremely low (<1–3 ppm total LREE, Fig. 8) in all glass-bearing experiments on MORB and AOC, except at the highest temperature when epidote is exhausted. Epidote forms a solid solution with allanite, indicating a demonstrable ability to accommodate LREE in its structure (e.g. Frei *et al.*, 2003). Analyses of epidote in our run products show elevated LREE, in one case readily analysable by EMPA (Supplementary Data file 5). For example, in a run on AOC at 900°C epidote contains 1000 ± 300 ppm Ce, 400 ± 100 ppm La, and 900 ± 300 ppm Nd. The corresponding epidote–melt partition coefficients are $D_{La} \approx 1500 \pm 600$, $D_{Ce} \approx 1200 \pm 400$ and $D_{Nd} \approx 700 \pm 300$ (Supplementary Data file 6). The observed concentrations of ΣLREE (La–Sm) are much lower than those required for allanite solubility (Fig. 8), confirming that this mineral was absent from our experiments in contrast to those of Hermann (2002*a*) and Klimm *et al.* (2008). We attribute this key difference to the relatively high doping levels of LREE used in those studies. In fact, the LREE partition coefficients between epidote and melt given above are higher than those for allanite at 900°C and 2·5 GPa (Klimm *et al.*, 2008) by a factor of ~2.

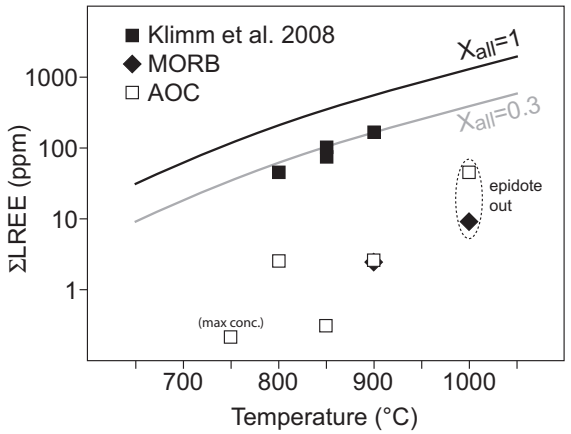

Fig. 8. Variation of log ΣLREE (La–Sm) in glasses versus temperature. Continuous curves are modelled ΣLREE using the allanite solubility equation (9) given by Klimm *et al.* (2008), for pure allanite ($X_{all} = 1$), and for $X_{all} = 0{\cdot}3$ [approximating the composition found by Klimm *et al.* (2008)]. The ΣLREE of our undoped experiments is significantly lower when compared with allanite-saturated experiments. (max conc.) refers to maximum measurement near detection limits, see Table 5.

It is logical to conclude that doping with LREE in the experiments of Hermann (2002*b*), Kessel *et al.* (2005*a*) and Klimm *et al.* (2008), where allanite was found to be the principal carrier for LREE + Th, simply pushed the composition of the allanite–epidote solid solution to the high LREE end-member, thereby increasing the overall level of LREE + Th in the glasses in the doped experiments. Additional evidence for the stability of allanite versus epidote can be drawn from field examples. Although allanites are found in some (ultra) high-pressure [(U)HP] terrains, they are typically restricted to REE-enriched rocks with alkaline affinities [as opposed to normal (N)-MORB], or Fe-gabbros (e.g. Tribuzio *et al.*, 1996; Hermann, 2002*b*; Spandler *et al.*, 2003). These rock types are not representative of average oceanic basaltic crust and, indeed, epidote–zoisite is much more common in exhumed (U)HP terrains (Enami *et al.*, 2004). It should be noted in that context that UHP terrains most often represent the un-molten, sub-solidus protolith of subducted crust, and allanite forms only above the solidus according to Klimm *et al.* (2008) (reaction: epidote = allanite + melt). Our experimental study suggests, however, that epidote would not change its composition appreciably above the solidus.

We conclude that the control on LREE contents of subduction zone melts of basalt is still an epidote-group mineral, but one much poorer in LREE than allanite. A simple test of this proposal is to use the solubility model of Klimm *et al.* (2008), but with the epidote compositions determined in our experiments (Fig. 8). These have considerably lower mole fractions of allanite (X_{all}), which leads to much lower levels of LREE in the melt according to equation (9) of Klimm *et al.* (2008). We use the epidote from the AOC 900°C run with the LREE

contents given in Supplementary Data file 5. In this run $X_{all} \approx 0{\cdot}008$; assuming ideal mixing this would equate to an LREE content in melts 125 times lower than if pure allanite were present in the residue. Inspection of Fig. 8 shows that this is indeed the case for this run: at 900°C Klimm *et al.* (2008) found $X_{all} \approx 0{\cdot}4$ and ΣLREE (La–Sm) in the melt of 168 ppm, whereas we have $X_{all} = 0{\cdot}008$ and ΣLREE = 2·7 ppm; that is, X_{all} is 53 times lower and ΣLREE 62 times lower in our experiment than in those of Klimm *et al.* (2008). The close correspondence between the observed X_{all} and melt LREE content in our experiments and those of Klimm *et al.* (2008) lends strong support to the notion that epidote-group minerals limit the flux of LREE from subducted basalt to the mantle wedge at temperatures below 900°C.

To employ the allanite solubility approach to better understand basalt-derived fluxes of LREE + Th (e.g. Plank *et al.*, 2009), we need a thermodynamic model of the allanite–epidote solid solution. In addition, we need to constrain the bulk-rock and fO_2 control on epidote–zoisite solid solutions and their respective stability fields. For example, the stability field of the zoisite endmember in MORB does not extend much beyond 2·5 GPa, 800°C or 3 GPa, 700°C (e.g. Schmidt & Poli, 1998; Poli *et al.*, 2009). Our experiments reveal that Fe^{3+}-bearing epidote may well be stable at much higher temperatures at 3 GPa. Hence X_{all} in epidote has the potential to vary significantly. It is also known that partition coefficients of LREE + Th, and possibly U, vary as a function of the epidote–zoisite solid solution (see, e.g. Frei *et al.*, 2003, 2004; Martin *et al.*, 2011). In the absence of any such data our experiments provide useful first constraints, demonstrating that negligible basalt-derived LREE + Th concentrations enter the arc basalt source region. Unless slab-top temperatures are much higher than existing models would suggest, LREE + Th enrichment in arc magmas must therefore originate from the sedimentary veneer.

Implications for arc basalt trace element geochemistry

Our experiments have a number of implications for the chemistry of the basalt-derived component added to the mantle wedge source of arc basalts. Although the tripartite model of the arc magma source reviewed by Elliott (2003) (Fig. 9) advocates an aqueous fluid as the key transporting agent of trace elements from the basaltic portion of the slab to the wedge, it is instructive to evaluate the potential for basalt-derived melts to affect the required chemical signal. It should be noted that although at super-critical or near super-critical conditions the distinction between fluid and melt disappears, there is still a relationship between total solutes in the fluid phase and temperature. At low temperatures, the composition and physical properties of the fluid phase will resemble those of an aqueous fluid, whereas at high temperatures they will resemble those of a hydrous melt (e.g. Hermann & Rubatto, 2014, fig. 11). Thus, our

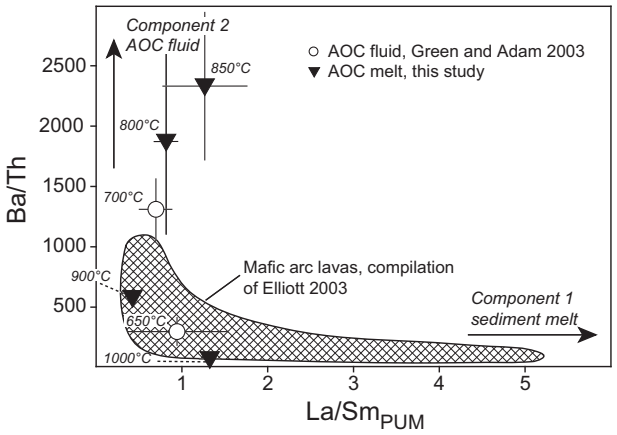

Fig. 9. $(La/Sm)_{PUM}$ versus Ba/Th for mafic arc lavas worldwide [compilation of Elliott (2003) shown in the hatched field]. Superimposed are the chemical compositions of the experimental glasses of this study, as well as the sub-solidus experiments of Green & Adam (2003). Barium/Th ratios are highest in our melts at 800–850°C from an AOC source, where epidote is present (retaining Th) but phengite (retaining Ba) is absent. Conversely, at low, sub-solidus temperatures, residual phengite will retain Ba and reduce Ba/Th in the fluids. Thus elevated Ba/Th is favoured by a narrow temperature interval between phengite-out and epidote-out.

data are principally also relevant for supercritical fluids that have the physical properties of a hydrous melt. Our basalt-derived melts approximate the composition of the total subduction component only in the case of sediment-starved arcs; sediment-derived melts will have different trace element chemistries because of their different bulk compositions, leading to different residual assemblages at high pressure, and initial trace element inventories. For this reason we compare directly the trace element composition of our experimental melts with basaltic arc lavas whose subduction component is thought to be dominated by material from the mafic crust (e.g. Tonga, Izu–Bonin, some Mariana islands; Elliott, 2003). Because our experimental starting materials were undoped, it is possible, for the first time, to make direct inferences about the melt flux from subducted basalt as a function of temperature based on analyses of trace elements in quenched experimental glasses.

Trace element contribution

Primitive upper mantle-normalized trace element patterns for melts derived from MORB and AOC exhibit several striking features (Fig. 5). First, the overall concentrations of trace elements, relative to PUM, increase with increasing temperature, although fractionation between adjacent elements decreases with increasing temperature. Thus the most 'spiky' trace element patterns are observed at the lowest temperatures. Second, the only elements with concentrations significantly higher (factor >3) than PUM at all temperatures, and therefore able to significantly modify the trace element chemistry of the mantle wedge, are the fluid-mobile elements (e.g. Cs, Rb, K, Ba, Sr, and U). This is

consistent with their enrichment even in sediment-starved arcs (e.g. Tonga, Izu–Bonin, some Mariana islands). Zirconium, Hf and Li are also surprisingly enriched in our partial melts (see below). Titanium, Nb and Ta enrichments exceed a factor of three only at the highest temperatures studied (>900°C). REE are lower than 3 × PUM except at 1000°C.

Sediment-starved arcs typically have low concentrations of many incompatible elements when compared with sediment-rich arcs, and exhibit low La/Sm and high Ba/Th, as well as Sr isotope ratios consistent with contributions from an altered MORB source. Elliott (2003) showed that the Ba/Th ratio of the basalt-derived component is in excess of 1000 with a $(La/Sm)_{PUM}$ of around unity (Fig. 5). This special characteristic of the arc geochemical signature has been traditionally ascribed to a 'fluid' phase from subducted mafic oceanic crust. However, similar characteristics are observed in our melts at 800–850°C from an AOC source in which residual epidote is present (retaining Th) but phengite (retaining Ba) is absent. The same is likely to be true for the 750°C AOC experiment, but exact Ba/Th and $(La/Sm)_{PUM}$ could not be determined because Th, La and Sm were below detection. At higher temperatures the increased Th content, allowed by the progressive breakdown of epidote, as well as increased melt fractions, reduces Ba/Th significantly (Fig. 5). At lower (sub-solidus) temperatures, the presence of residual phengite will retain Ba and reduce Ba/Th in the fluid. This is readily apparent from the 650°C, 3 GPa sub-solidus fluid analyses of Green & Adam (2003). At 700°C the Ba/Th of sub-solidus fluids approaches those measured in our supra-solidus experiments, probably because the solubility of phengite and other silicates is enhanced in near-solidus fluids (e.g. Manning *et al.*, 2010). [Note in that context that Green & Adam (2003) used a doped starting material. Whether the absolute Ba/Th values given by Green & Adam (2003) truly approximate nature requires undoped experiments.]

Our results suggest that the Ba/Th and $(La/Sm)_{PUM}$ characteristics of the 'fluid' component can be delivered by a wet melt of basalt (Fig. 9). Further complexity in Ba is introduced across the transition from sub- to supercritical behavior, as noted above. However, by far the greatest influence on Ba/Th ratios of melts is the presence or absence of phengite and epidote. Epidote stability is complex, as discussed above. Phengite stability, in turn, is primarily a function of bulk K_2O and H_2O, given that there is a strong relationship between $X_{phengite}$ (the only host of K_2O at sub-arc conditions), H_2O and the degree of melting (e.g. Schmidt *et al.*, 2004; Skora & Blundy, 2010). In our water-rich experiments, the Ba/Th ratio of melts supplied by the slab basalt end-member is controlled primarily by temperature, with the highest ratios being generated in the narrow window between exhaustion of phengite (at the solidus) and exhaustion of epidote (melted out above the solidus, at ~900°C). This window lies between 750–800 and 850°C (Fig. 9).

It is also worth noting that our sub-solidus, K-poor MORB run product contains epidote but no phengite, probably because the very low initial potassium content is fully dissolved in the fluid phase (discussed above). If this is generally the case, then Ba lacks a host in the sub-solidus mineral assemblage of subducted MORB at these conditions and may also be concentrated in the fluid phase. In contrast, Th will be retained by residual epidote and so fluids equilibrated with K-poor MORB at sub-solidus conditions may also have high Ba/Th ratios. It is therefore conceivable that fluids derived from lower parts of the subducted basalt, and equilibrated with unaltered MORB at sub-solidus conditions, as well as partial melt from the uppermost AOC are jointly responsible for the high Ba/Th ratios observed in sediment starved arcs. Our experiments show how effective epidote can be at keeping Ba/Th high and La/Sm low.

The tendency of our melts to show elevated Zr/Nd (range 10–1070), Hf/Sm (range 1–60), and Li/Y (range 3–80) ratios (Fig. 5) may at first seem paradoxical given that arc basalts do not show positive anomalies for these elements. Using the same compilation as Elliott (2003) for the most mafic Izu–Bonin and Tonga lavas, these ratios are closer to 7 ± 1 (Zr/Hf), $0{\cdot}6 \pm 0{\cdot}1$ (Hf/Sm) and $0{\cdot}4 \pm 0{\cdot}1$ (Li/Y). However, the trace element ratios of the added slab component are mirrored in arc basalts only when the elements of interest are not incorporated significantly into mantle minerals (e.g. Ba/Th). Zirconium, Hf and Li, however, are only modestly incompatible in mantle minerals (pyroxene, olivine). Studies such as that of Stolper & Newman (1994) have quantified the exchange of elements with the mantle wedge and concluded that all but the most incompatible elements are likely to equilibrate with it. Hence, we suggest that Zr, Hf and Li can be significantly modified by equilibration with the mantle wedge, to the extent that they no longer provide a clear insight into slab processes.

Finally, we note that melts derived from the basaltic portion of the slab have elevated U/Th ratios. This will lead to isotopic disequilibrium between the activities of ^{238}U and ^{230}Th that will be retained in the melt on timescales less than five half-lives of ^{230}Th (i.e. 350 kyr). An activity excess of ^{238}U over ^{230}Th is a characteristic of many sediment-starved arcs (e.g. McDermott & Hawkesworth, 1991). For example, in the Marianas the maximum ^{238}U activity excess over ^{230}Th observed by Elliott *et al.* (1997) and Avanzinelli *et al.* (2012) is ~1·6 [also see Elliott (2003) for a compilation of high ^{238}U activity excess over ^{230}Th]. Such a value is consistent with basalt-derived melts generated at 800–850°C from AOC, although we note that our source-normalized U/Th ratios are poorly constrained owing to analytical limitations.

CONCLUSIONS

Through a series of experiments conducted at sub-arc *P–T* conditions (750–1000°C, 3 GPa) in the presence of

excess water, we show that the temperature and composition of the down-going oceanic crust (pristine MORB versus AOC) can have a profound effect on the sub-arc phase assemblage and geochemistry, and therefore the resulting slab contribution to arc magma geochemistry. Notably, an order of magnitude elevated potassium content in AOC over MORB shifts the water-saturated basaltic solidus to lower temperature ($\sim$750°C AOC, 825 $\pm$ 25°C MORB). Just above the solidus, run products texturally indicate the presence of two liquids: an aqueous fluid with quench 'fish eggs', and a vesicular hydrous melt. With increasing temperature, the second vapour phase diminishes and disappears across the solvus. Further experimentation at varying P, X_{H2O} is needed to constrain the solvi and second critical endpoints for AOC and MORB.

For slab-top temperature estimates from recent subduction models (e.g. Syracuse *et al.*, 2010), our study confirms the likelihood that melt $\pm$ fluid, particularly from an altered (high-K_2O) oceanic basalt protolith, can transport important trace elements to the sources of arc magmas. Slab-top temperature imparts an important control on trace element concentrations in the melt and the ratios of key element pairs. In particular, oceanic crust can contribute melts with high ratios of Ba/Th and U/Th under conditions at which residual phengite is absent but epidote is present. The results from our undoped starting materials demonstrate the primacy of residual epidote as opposed to the LREE-rich allanite of previous, doped experimental studies.

ACKNOWLEDGEMENTS

This research was based in part on a Masters dissertation by L.B.C. at the University of Bristol. We thank the workshop at Bristol for assistance with the piston cylinders; S. Kearns and B. Buse for help with the SEM and EMPA at Bristol; EIMF staff at the University of Edinburgh for help with SIMS analysis, and M. Guillong for help with the LA-ICP-MS at ETH. We would like to thank C. Till and an anonymous reviewer for helpful comments on an earlier version of this paper. The constructive reviews of J. G. Prouteau, J. Adam, C. Spandler, and J. Hermann (Editor) have further improved our paper, and were greatly appreciated.

FUNDING

This work was supported by grants from the National Environmental Research Council (NE/G016615/1), the European Research Council (CRITMAG), and a Wolfson Research Merit Award to J.B., and a Swiss National Science Foundation Ambizone grant (PZ00P2_142575) to S.S.

SUPPLEMENTARY DATA

Supplementary data for this paper are available at *Journal of Petrology* online.

REFERENCES

Adam, J., Green, T., Sie, S. & Ryan, C. (1997). Trace element partitioning between aqueous fluids, silicate melts and minerals. *European Journal of Mineralogy* **9**, 569–584.

Alt, J., Anderson, T. & Bonnell, L. (1989). The geochemistry of sulfur in a 1·3 km section of hydrothermally altered oceanic crust, DSDP Hole 504B. *Geochimica et Cosmochimica Acta* **53**, 1011–1023.

Avanzinelli, R., Prytulak, J., Skora, S., Heumann, A., Koetsier, G. & Elliott, T. (2012). Combined ^{238}U–^{230}Th and ^{235}U–^{231}Pa constraints on the transport of slab-derived material beneath the Mariana Islands. *Geochimica et Cosmochimica Acta* **92**, 308–328.

Bach, W., Peucker-Ehrenbrink, B., Hart, S. R. & Blusztajn, J. S. (2003). Geochemistry of hydrothermally altered oceanic crust: DSDP/ODP Hole 504B—Implications for seawater–crust exchange budgets and Sr- and Pb-isotopic evolution of the mantle. *Geochemistry, Geophysics, Geosystems* **4**, 1–29.

Barker, F. (1979). Trondhjemite: Definition, environment and hypotheses of origin. In: Barker, F. (ed.) *Trondhjemites, Dacites, and Related Rocks*. Elsevier, pp. 1–12.

Bougault, H. & Cambon, P. (1979). Trace elements: Fractional crystallization and partial melting processes, heterogeneity of upper mantle material. *Initial Reports of the Deep Sea Drilling Project* **46**, 247–251.

Cooper, L. B., Ruscitto, D. M., Plank, T., Wallace, P. J., Syracuse, E. M. & Manning, C. E. (2012). Global variations in H_2O/Ce: 1. Slab surface temperatures beneath volcanic arcs. *Geochemistry, Geophysics, Geosystems* **13**, 1–27.

Cottrell, E. & Kelley, K. A. (2011). The oxidation state of Fe in MORB glasses and the oxygen fugacity of the upper mantle. *Earth and Planetary Science Letters* **305**, 270–282.

Devey, C. W., Garbe-Schönberg, C.-D., Stoffers, P., Chauvel, C. & Mertz, D. F. (1994). Geochemical effects of dynamic melting beneath ridges: Reconciling major and trace element variations in Kolbeinsey (and global) mid-ocean ridge basalt. *Journal of Geophysical Research* **99**, 9077–9095.

Droop, G. (1987). A general equation for estimating Fe^{3+} concentrations in ferromagnesian silicates and oxides from microprobe analyses, using stoichiometric criteria. *Mineralogical Magazine* **51**, 431–435.

Dungan, M., Rhodes, J., Long, P., Blanehard, D., Brannon, J. & Rodgers, K. (1979). Petrology and geochemistry of basalts from Site 396, Legs 45 and 46. *Initial Reports of the Deep Sea Drilling Project* **46**, 89–113.

Elliott, T. (2003). Geochemical tracers of the slab. In: Eiler, J. (ed.) *Inside the Subduction Factory. American Geophysical Union, Geophysical Monograph Series* **138**, 23–45.

Elliott, T., Plank, T. & Zindler, A. (1997). Element transport from slab to volcanic front at the Mariana arc. *Journal of Geophysical Research* **102**, 14991–15019.

Emmermann, R. & Puchelt, H. (1979). Abundances of rare earths and other trace elements, Leg 46 basalts (DSDP). *Initial Reports of the Deep Sea Drilling Project* **46**, 241–245.

Enami, M., Liou, J. & Mattinson, C. (2004). Epidote minerals in high *P*/*T* metamorphic terranes: subduction zone and high- to ultrahigh-pressure metamorphism. In: Liebscher, A. & Franz, G. (eds) *Epidotes. Mineralogical Society of America and Geochemical Society, Reviews in Mineralogy and Geochemistry* **56**, 347–398.

Frei, D., Liebscher, A., Wittenberg, A. & Shaw, C. S. J. (2003). Crystal chemical controls on rare earth element partitioning between epidote-group minerals and melts: an experimental and theoretical study. *Contributions to Mineralogy and Petrology* **146**, 192–204.

Frei, D., Liebscher, A., Franz, G. & Dulski, P. (2004). Trace element geochemistry of epidote minerals. In: Liebscher, A. & Franz, G. (eds) *Epidotes. Mineralogical Society of America and Geochemical Society, Reviews in Mineralogy and Geochemistry* **56**, 553–605.

Gillis, K. & Robinson, P. (1988). Distribution of alteration zones in the upper oceanic crust. *Geology* **16**, 262–266.

Green, T. H. & Adam, J. (2003). Experimentally-determined trace element characteristics of aqueous fluid from partially dehydrated mafic oceanic crust at 3·0 GPa, 650–700°C. *European Journal of Mineralogy* **15**, 815–830.

Guillong, M., Meier, D. L. Allan, M. M., Heinrich, C. A. & Yardley, B. W. D. (2008). SILLS: A MATLAB-based program for the reduction of laser ablation ICP-MS data of homogeneous materials and inclusions. In: Sylvester, P. (ed.) *Laser Ablation ICP-MS in the Earth Sciences: Current Practices and Outstanding Issues. Mineralogical Association of Canada, Short Course* **40**, 328–333.

Hermann, J. (2002a). Allanite: thorium and light rare earth element carrier in subducted crust. *Chemical Geology* **192**, 289–306.

Hermann, J. (2002b). Experimental constraints on phase relations in subducted continental crust. *Contributions to Mineralogy and Petrology* **143**, 219–235.

Hermann, J. & Green, D. H. (2001). Experimental constraints on high pressure melting in subducted crust. *Earth and Planetary Science Letters* **188**, 149–168.

Hermann, J. & Rubatto, D. (2014). Subduction of continental crust to mantle depth: geochemistry of ultrahigh-pressure rocks. In: Rudnick, R. L. (ed.) *Treatise on Geochemistry 4: The Crust*, 2nd edn. Elsevier, pp. 309–340.

Hermann, J. & Spandler, C. J. (2008). Sediment melts at sub-arc depths: an experimental study. *Journal of Petrology* **49**, 717–740.

Hermann, J., Spandler, C., Hack, A. & Korsakov, A. (2006). Aqueous fluids and hydrous melts in high-pressure and ultra-high pressure rocks: Implications for element transfer in subduction zones. *Lithos* **92**, 399–417.

Hofmann, A. W. (1988). Chemical differentiation of the Earth: the relationship between mantle, continental crust, and oceanic crust. *Earth and Planetary Science Letters* **90**, 297–314.

Humphris, S. & Thompson, G. (1978). Hydrothermal alteration of oceanic basalts by seawater. *Geochimica et Cosmochimica Acta* **42**, 107–125.

Kagi, R., Muntener, O., Ulmer, P. & Ottolini, L. (2005). Piston-cylinder experiments on H_2O undersaturated Fe-bearing systems: An experimental setup approaching fO_2 conditions of natural calc-alkaline magmas. *American Mineralogist* **90**, 708–717.

Kelley, K. A., Plank, T., Ludden, J. & Staudigel, H. (2003). Composition of altered oceanic crust at ODP Sites 801 and 1149. *Geochemistry, Geophysics, Geosystems* **4**, 1–21.

Kessel, R., Schmidt, M. W., Ulmer, P. & Pettke, T. (2005a). Trace element signature of subduction-zone fluids, melts and supercritical liquids at 120–180 km depth. *Nature* **437**, 724–727.

Kessel, R., Ulmer, P., Pettke, T., Schmidt, M. W. & Thompson, A. B. (2005b). The water–basalt system at 4 to 6 GPa: Phase relations and second critical endpoint in a K-free eclogite at 700 to 1400°C. *Earth and Planetary Science Letters* **237**, 873–892.

Klemme, S., Blundy, J. & Wood, B. (2002). Experimental constraints on major and trace element partitioning during partial melting of eclogite. *Geochimica et Cosmochimica Acta* **66**, 3109–3123.

Klimm, K., Blundy, J. D. & Green, T. H. (2008). Trace element partitioning and accessory phase saturation during H_2O-saturated melting of basalt with implications for subduction zone chemical fluxes. *Journal of Petrology* **49**, 523–553.

Kogiso, T., Tatsumi, Y. & Nakano, S. (1997). Trace element transport during dehydration processes in the subducted oceanic crust: 1. Experiments and implications for the origin of ocean island basalts. *Earth and Planetary Science Letters* **148**, 193–205.

Konzett, J., Frost, D. J., Proyer, A. & Ulmer, P. (2007). The Ca-Eskola component in eclogitic clinopyroxene as a function of pressure, temperature and bulk composition: an experimental study to 15 GPa with possible implications for the formation of oriented SiO_2-inclusions in omphacite. *Contributions to Mineralogy and Petrology* **155**, 215–228.

Lambert, I. & Wyllie, P. (1972). Melting of gabbro (quartz eclogite) with excess water to 35 kilobars, with geological applications. *Journal of Geology* **80**, 693–708.

Manning, C. (2004). The chemistry of subduction-zone fluids. *Earth and Planetary Science Letters* **223**, 1–16.

Manning, C. E., Antignano, A. & Lin, H. A. (2010). Premelting polymerization of crustal and mantle fluids, as indicated by the solubility of albite + paragonite + quartz in H_2O at 1 GPa and 350–620°C. *Earth and Planetary Science Letters* **292**, 325–336.

Martin, L. A. J., Wood, B. J., Turner, S. & Rushmer, T. (2011). Experimental measurements of trace element partitioning between lawsonite, zoisite and fluid and their implication for the composition of arc magmas. *Journal of Petrology* **52**, 1049–1075.

McDade, P., Wood, B. J., Van Westrenen, W., Brooker, R., Gudmundsson, G., Soulard, H., Najorka, J. & Blundy, J. (2002). Pressure corrections for a selection of piston-cylinder cell assemblies. *Mineralogical Magazine* **66**, 1021–1028.

McDermott, F. & Hawkesworth, C. (1991). Th, Pb, and Sr isotope variations in young island arc volcanics and oceanic sediments. *Earth and Planetary Science Letters* **104**, 1–15.

McMillan, P. F. & Holloway, J. R. (1987). Water solubility in aluminosilicate melts. *Contributions to Mineralogy and Petrology* **97**, 320–332.

Melson, W. (1968). Volcanism and metamorphism in the Mid Atlantic Ridge, 22°N latitude. *Journal of Geophysical Research* **73**, 5925–5941.

Molina, J. & Poli, S. (2000). Carbonate stability and fluid composition in subducted oceanic crust: an experimental study on H_2O–CO_2-bearing basalts. *Earth and Planetary Science Letters* **176**, 295–310.

Mottl, M. (1983). Metabasalts, axial hot springs, and the structure of hydrothermal systems at mid-ocean ridges. *Geological Society of America Bulletin* **94**, 161–180.

Pearce, N. J. G., Perkins, W. T., Westgate, J. A., Gorton, M. P., Jackson, S. E., Neal, C. R. & Chenery, S. P. (1997). A compilation of new and published major and trace element data for NIST SRM 610 and NIST SRM 612 glass reference materials. *Geostandards Newsletter* **21**, 115–144.

Pertermann, M. & Hirschmann, M. M. (2003). Anhydrous partial melting experiments on MORB-like eclogite: phase relations, phase compositions and mineral–melt partitioning of major elements at 2–3 GPa. *Journal of Petrology* **44**, 2173–2201.

Plank, T., Cooper, L. B. & Manning, C. E. (2009). Emerging geothermometers for estimating slab surface temperatures. *Nature Geoscience* **2**, 611–615.

Poli, S., Franzolin, E., Fumagalli, P. & Crottini, A. (2009). The transport of carbon and hydrogen in subducted oceanic crust: An experimental study to 5 GPa. *Earth and Planetary Science Letters* **278**, 350–360.

Prouteau, G. & Scaillet, B. (2013). Experimental constraints on sulphur behaviour in subduction zones: implications for TTG and adakite production and the global sulphur cycle since the Archean. *Journal of Petrology* **54**, 183–213.

Prouteau, G., Scaillet, B., Pichavant, M. & Maury, R. (1999). Fluid-present melting of oceanic crust in subduction zones. *Geology* **27**, 1111–1114.

Prouteau, G., Scaillet, B., Pichavant, M. & Maury, R. (2001). Evidence for mantle metasomatism by hydrous silicic melts derived from subducted oceanic crust. *Nature* **410**, 197–200.

Rapp, R. P. & Watson, E. B. (1995). Dehydration melting of metabasalt at 8–32 kbar: implications for continental growth and crust–mantle recycling. *Journal of Petrology* **36**, 891–931.

Ryabchikov, I. D., Miller, C. & Mirwald, P. W. (1996). Composition of hydrous melts in equilibrium with quartz eclogites. *Mineralogy and Petrology* **58**, 101–110.

Sato, H., Aoki, K.-I., Okamoto, K. & Fujita, B.-Y. (1979). Petrology and chemistry of basaltic rocks from hole 396B, IPOD/DSDP leg 46. *Inital Reports of the Deep Sea Drilling Project* **46**, 115–141.

Schmidt, M. (1996). Experimental constraints on recycling of potassium from subducted oceanic crust. *Science* **272**, 1927–1930.

Schmidt, M. W. & Poli, S. (1998). Experimentally based water budgets for dehydrating slabs and consequences for arc magma generation. *Earth and Planetary Science Letters* **163**, 361–379.

Schmidt, M. W. & Poli, S. (2014). Devolatilization during subduction. In: Rudnick, R. L. (ed.) *Treatise on Geochemistry 4: The Crust*, 2nd edn. Elsevier, pp. 669–701.

Schmidt, M. W., Vielzeuf, D. & Auzanneau, E. (2004). Melting and dissolution of subducting crust at high pressures: the key role of white mica. *Earth and Planetary Science Letters* **228**, 65–84.

Seyfried, W., Berndt, M. & Seewald, J. (1988). Hydrothermal alteration processes at mid-ocean ridges: constraints from diabase alteration experiments, hot spring fluids and composition of the oceanic crust. *Canadian Mineralogist* **26**, 787–804.

Skora, S. & Blundy, J. (2010). High-pressure hydrous phase relations of radiolarian clay and implications for the involvement of subducted sediment in arc magmatism. *Journal of Petrology* **51**, 2211–2243.

Skora, S. & Blundy, J. (2012). Monazite solubility in hydrous silicic melts at high pressure conditions relevant to subduction zone metamorphism. *Earth and Planetary Science Letters* **321–322**, 104–114.

Spandler, C. & Pirard, C. (2013). Element recycling from subducting slabs to arc crust: A review. *Lithos* **170–171**, 208–223.

Spandler, C., Hermann, J., Arculus, R. & Mavrogenes, J. (2003). Redistribution of trace elements during prograde metamorphism from lawsonite blueschist to eclogite facies; implications for deep subduction-zone processes. *Contributions to Mineralogy and Petrology* **146**, 205–222.

Staudigel, H. & Plank, T. (1996). Geochemical fluxes during seafloor alteration of the basaltic upper oceanic crust: DSDP Sites 417 and 418. In: Bebout, G. E., Scholl, D. W., Kirby, S. H. & Platt, J. P. (eds) *Subduction Top to Bottom. American Geophysical Union, Geophysical Monograph Series* **96**, 19–38.

Staudigel, H., Hart, S. & Richardson, S. (1981a). Alteration of the oceanic crust: processes and timing. *Earth and Planetary Science Letters* **52**, 311–327.

Staudigel, H., Muehlenbachs, K., Richardson, S. H. & Hart, S. R. (1981b). Agents of low temperature ocean crust alteration. *Contributions to Mineralogy and Petrology* **77**, 150–157.

Stolper, E. & Newman, S. (1994). The role of water in the petrogenesis of Mariana trough magmas. *Earth and Planetary Science Letters* **121**, 293–325.

Sun, S.-S. & McDonough, W. F. (1989). Chemical and isotopic systematics of oceanic basalts: implications for mantle composition and processes. In: Saunders, A. D. & Norry, M. J. (eds) *Magmatism in the Ocean Basins. Geological Society, London, Special Publications* **42**, 313–345.

Syracuse, E. M. & Abers, G. A. (2006). Global compilation of variations in slab depth beneath arc volcanoes and implications. *Geochemistry, Geophysics, Geosystems* **7**, 1–18.

Syracuse, E. M., van Keken, P. E. & Abers, G. A. (2010). The global range of subduction zone thermal models. *Physics of the Earth and Planetary Interiors* **183**, 73–90.

Thompson, G. (1983). Basalt–seawater interaction. In: Rona, P. A., Boström, K., Laubier, L. & Smith, K. L. (eds) *Hydrothermal Processes at Seafloor Spreading Centers. NATO Conference Series IV: Marine Sciences* **12P**, 225–278.

Tribuzio, R., Messiga, B., Vannucci, R. & Bottazzi, P. (1996). Rare earth element redistribution during high-pressure–low-temperature metamorphism in ophiolitic Fe-gabbros (Liguria, northwestern Italy): Implications for light REE. *Geology* **24**, 711–714.

Truckenbrodt, J., Ziegenbein, D. & Johannes, W. (1997). Redox conditions in piston cylinder apparatus: The different behavior of boron nitride and unfired pyrophyllite assemblies. *American Mineralogist* **82**, 337–344.

Ulmer, P. & Trommsdorff, V. (1995). Serpentine stability to mantle depths and subduction-related magmatism. *Science* **268**, 858–861.

Van Keken, P. E., Hacker, B. R., Syracuse, E. M. & Abers, G. A. (2011). Subduction factory: 4. Depth-dependent flux of H_2O from subducting slabs worldwide. *Journal of Geophysical Research* **116**, 1–15.

Van Keken, P. E., Kiefer, B. & Peacock, S. M. (2002). High-resolution models of subduction zones: Implications for mineral dehydration reactions and the transport of water into the deep mantle. *Geochemistry, Geophysics, Geosystems* **3**, 1–20.

Yasuda, A., Fujii, T. & Kurita, K. (1994). Melting phase relations of an anhydrous mid-ocean ridge basalt from 3 to 20 GPa: Implications for the behavior of subducted oceanic crust in the mantle. *Journal of Geophysical Research* **99**, 9401–9414.